LAMINAR TURBULENT TRANSITION IN A HYPERSONIC BOUNDARY LAYER

RECEPTIVITY AND INSTABILITY PRE-HISTORY

A. V. Fedorov

Moscow Institute of Physics and Technology
16 Gagarin Street, Zhukovski, Moscow Region, 140160
Russia

European Office of Aerospace Research and Development
Special Project SPC-96-4024
Contract F61708-96-W0196

July 1997

REPORT DOCUMENTATION PAGE

Form Approved OMB No. 0704-0188

1. AGENCY USE ONLY (Leave blank)	2. REPORT DATE	3. REPORT TYPE AND DATES COVERED
		Final Report

4. TITLE AND SUBTITLE

Laminar-Turbulent Transition in a Hypersonic Boundary Layer

5. FUNDING NUMBERS

F6170896W0196

6. AUTHOR(S)

Dr. Alexander Fedorov

7. PERFORMING ORGANIZATION NAME(S) AND ADDRESS(ES)

Moscow Inst. of Physics and Technology
16 Gagarin St,
Zhukovsky 140160
Russia

8. PERFORMING ORGANIZATION REPORT NUMBER

N/A

9. SPONSORING/MONITORING AGENCY NAME(S) AND ADDRESS(ES)

EOARD
PSC 802 BOX 14
FPO 09499-0200

10. SPONSORING/MONITORING AGENCY REPORT NUMBER

SPC 96-4024

11. SUPPLEMENTARY NOTES

12a. DISTRIBUTION/AVAILABILITY STATEMENT

Approved for public release; distribution is unlimited.

12b. DISTRIBUTION CODE

A

13. ABSTRACT (Maximum 200 words)

This report results from a contract tasking Moscow Inst. of Physics and Technology as follows: The contractor will perform research in accordance with contractor's proposal entitled, 'Laminar-Turbulent Transitin in an Hypersonic Boundary Layer.'

14. SUBJECT TERMS

Aircraft Subsystem, Aircraft Structures

15. NUMBER OF PAGES

71

16. PRICE CODE

N/A

17. SECURITY CLASSIFICATION OF REPORT	18. SECURITY CLASSIFICATION OF THIS PAGE	19. SECURITY CLASSIFICATION OF ABSTRACT	20. LIMITATION OF ABSTRACT
UNCLASSIFIED	UNCLASSIFIED	UNCLASSIFIED	UL

Abstract

This report addresses the initial phase of hypersonic boundary-layer transition comprising excitation of unstable normal modes (receptivity problem) and their downstream evolution from receptivity regions to the instability growth onset (instability pre-history problem). It is shown that this phase is more complicated than in subsonic and moderate supersonic cases due to the following features of the disturbance field: (1) the first and second modes are synchronized with acoustic waves near the body nose region; (2) further downstream the first mode is synchronized with entropy/vorticity waves; (3) near the instability growth onset the first mode is synchronized with the second mode. Disturbance behavior in the synchronism regions (2) and (3) are studied using the multiple-mode method, which accounts for interaction between modes of discrete and continuous spectrum due to nonparallel effects of the mean flow. It is shown that vorticity/entropy waves are partially swallowed by the boundary layer and effectively generate the first mode due to Synchronism (2). This mechanism can compete with the leading edge receptivity to the freestream acoustic waves in cases of "quiet" freestream conditions and conical body configurations. Spectrum topology and interaction between the first and second modes due to Synchronism (3) is studied using asymptotic and numerical analyses. Branch points of the discrete spectrum were identified. It is shown that near the branch points normal modes have singular behavior. The inter-mode exchange rule coupling input and output characteristics of the first and second modes crossing the branch point vicinity was established. Combination of the receptivity estimates related to Synchronism (2) and the inter-mode exchange rule related to Synchronism (3) allows the evaluation of instability initial amplitudes required for the PSE calculations of the transition onset point. That makes feasible an amplitude method coupling receptivity and stability problems. Results of analyses are compared with experimental observations in the AEDC Tunnel B on sharp cones at the freestream Mach number $M = 8$. Possible ways of experimental investigation of hypersonic receptivity and instability pre-history are discussed.

Table of contents

Nomenclature

Latin symbols

$\vec{A}$	eigenvector of direct problem
$\vec{B}$	eigenvector of conjugate problem
c	amplitude coefficient or phase speed
$F = \omega\nu_e / U_e^2$	frequency parameter
G_0	stability equation matrix
L	reference streamwise length
M	Mach number
P	mean-flow pressure
Q	mass flux disturbance amplitude
p	pressure disturbance
$R = \sqrt{U_e^* x^* / \nu_e^*}$	Reynolds number based on the boundary-layer scale $\sqrt{\nu_e^* x^* / U_e^*}$
$R_L = \sqrt{U_e^* L^* / \nu_e^*}$	Reynolds number based on the boundary-layer scale $\sqrt{L^* \nu_e^* / U_e^*}$
T	mean-flow temperature
t	time
U , V	mean-flow streamwise and vertical velocity
u, v	disturbance of x - and y-velocity component
$x = x^* / L^*$	streamwise coordinate
$y = y^* / \delta$	coordinate normal to the wall surface

Greek symbols

α	x-component of the wavenumber vector
$\delta = \sqrt{L^* \nu_e^* / U_e^*}$	boundary-layer scale
δ^*	boundary-layer displacement thickness

$\varepsilon = 1/R_L$	small parameter
$\eta = y/\sqrt{x}$	boundary-layer coordinate
μ	viscosity
ν	kinematic viscosity
θ	temperature disturbance
σ	Prandtl number
$\omega = \omega^* \delta / U_e^*$	angular frequency
$\vec{\Psi}$	disturbance vector

Subscripts

ad	adiabatic wall
asterisk	synchronism between entropy/vorticity waves and the first mode
b	branch point
cr	critical
e	upper boundary layer edge or entropy wave
i	imaginary part
in	initial
r	real part
v	vorticity wave
w	wall

Superscripts

bar	complex conjugate value
asterisk	dimensional value

Abbreviations

PSE	parabolized stability equations
Im	imaginary part
Re	real part

List of figures

1. Introduction

Laminar-turbulent transition in a hypersonic boundary layer causes the significant increase in heat transfer and skin friction. Since the aerodynamic coefficients of hypersonic vehicles are sensitive to these changes, the ability to predict the transition location and simulate the transition zone is important in the design and optimization of aerospace vehicles [1]. The stability, control, and structural design are also affected due to the increased thermal and aerodynamic loading. Recent technology does not provide accurate prediction of transition due to the complexity of this phenomenon. Uncertainty in transition location leads to diminished vehicle performance, primarily because of the additional weight of the thermal protection [2]. These factors stimulate further theoretical and experimental studies of hypersonic transition [3].

For flight and quiet wind tunnel conditions, freestream disturbances and perturbations generated by hypersonic body surfaces are normally small in a frequency band related to the boundary-layer transition process. In this case, the initial phase of transition comprises excitation of unstable normal modes (receptivity problem), their downstream amplification (stability problem) and non-linear mechanisms, which trigger transition at critical amplitudes of the boundary-layer disturbances (transition onset problem) [4], [5].

Linear stability theory allows the identification of unstable modes and prediction of their downstream growth [3], [6], [7]. Stability theory is well developed for subsonic and moderate supersonic boundary layers [8]. Its results are consistent with many experiments [9]-[11]. Good progress has been recently made in receptivity at subsonic speeds [12]-[18]. Combination of the receptivity theory with stability analysis based on the parabolized stability equations (PSE) [19], [20] makes feasible an amplitude method [21] coupling the external disturbance characteristics with the transition onset locus. Much progress toward the subsonic and moderate supersonic transition prediction is partially due to the fact that

the boundary-layer disturbance spectrum is relatively simple in these cases. *I.e.* unstable normal modes of discrete spectrum has no branch points, turning points and other singularities. For example, transition on subsonic/supersonic cones, flat plates, axisymmetric bodies at zero angle of attack and airfoils is due to excitation and downstream amplification of the Tollmien-Schlichting waves, which belong to the first normal mode according to Mack's classification [22]. Other modes are stable and their eigenvalues are essentially different from the first mode. In this case, interaction between Tollmien-Schlichting waves and other normal modes can be neglected in the instability growth prediction. Such a single-mode approach is currently used in the e^N -method [7] and the PSE analysis [20].

In contrast to moderate supersonic flows, the initial phase of hypersonic transition (at Mach numbers larger than 4) reveals the following new features:

(i) Besides the first mode, the second and higher modes coexist in the boundary layer. They belong to the family of trapped acoustic normal waves. Once the second mode sets in, it becomes the dominant instability since its growth rate tends to exceed that of the first mode. For insulated surfaces, this occurs for Mach numbers $M > 4$. For cooled surfaces, the second mode can dominate at even lower Mach number. The existence of the second mode instability was established by the experiments of Kendall [23], Demetriades [24], and Stetson *et al.* [25], [26]. The Mach 8 stability and transition experiments [25] (see also [26]) for the boundary layer on a sharp cone indicated that the unstable high-frequency second mode plays a major role in the conical boundary-layer transition. These data are consistent with the second mode stability calculations [27]-[29]. The linear stability theory is in a qualitative agreement with the conical boundary layer experiments. However quantitative discrepancy still exists. Stetson and Kimmel [26] noted that "for the linearized stability calculations, there is concern about the effects of the large second mode disturbances and the early presence of the nonlinear disturbances. For the experimental data there is concern about the effects of the uncontrolled freestream environment and the limitations of the hot-wire anemometry

data." In addition, this discrepancy may relate to the disturbance spectrum singularities near the branch points discussed in Section 4.

(ii) The second mode instability is associated with synchronization between the first and second modes [30], [31]. Near the synchronism point, the eigenvalue spectrum splits into two branches. In the vicinity of branch points, the eigenmode decomposition is not valid and should be replaced by a local solution. Asymptotic analysis of this solution reveals a strong exchange between modes due to nonparallel effect [32]. This finding leads to the conclusion that, instead of a single-mode stability analysis recently used in the transition prediction technology, a multiple-mode analysis is required to account for interaction between normal modes, particularly between the first and second modes.

(ii) Stability and transition experiments on a planar boundary layer [33] showed that the low frequency disturbances are growing despite the fact that the linear stability numerical results indicated the first mode disturbances should be stable [29]. Stetson *et al.* [33] reported: "There was no evidence of any second mode harmonics in the planar boundary layer. The major disturbances are the low frequency disturbances which are growing in a frequency band expected to be stable." These results are consistent with the flat plate results of Kendall [23] obtained at Mach numbers 3., 4.5, and 5.6. Kendall reported that "fluctuations of all frequencies were observed to grow monotonically larger in the region of a boundary layer extending from the flat plate leading edge to the predicted location of instability; *i.e.* in a region where no growth was expected". Mack [34] developed a forcing theory, which was successfully applied to Kendall's Mach 4.5 planar data. However Mack noted "the major difficulty in the use of the forcing theory is that forced disturbances are distinct from free disturbances, and the process by which the former becomes the latter is unknown". This coupling between freestream (external) sound and normal modes of planar supersonic boundary layer has been theoretically studied in [32], [35]. It was found that the first and second modes are synchronized with acoustic waves near the leading edge of a flat plate, *i.e.* frequency and wavenumber of the normal mode coincide with those of an external acoustic

wave. That causes a strong excitation of the normal modes by freestream noise through the mechanism, which is qualitatively different from the subsonic case studied in [13], [18].

(iii) For low supersonic Mach numbers, the dominant boundary-layer disturbances have relatively low frequency. The wind tunnel freestream has intensive acoustic disturbances at the corresponding frequency band and provides large initial amplitudes for normal modes at the instability growth onset associated with the lower neutral branch. The major source of these disturbances is due to radiation of acoustic waves by the turbulent boundary layer on the wind tunnel nozzle walls. That causes transition Reynolds numbers in conventional supersonic wind tunnels to be significantly lower than ones in flight conditions. Hypersonic transition wind tunnel testing presents a different situation [26]. If the dominant boundary-layer disturbances belong to the second mode, they have relatively high frequency. Since most of acoustic energy is concentrated in the low frequency band, the noise intensity rapidly decreases with increasing frequency until the signal is lost in the instrumentation noise. Therefore, the "noisy" hypersonic wind tunnel can be "quiet" for the second mode frequency band. In this situation, freestream turbulence (vortical disturbances) and entropy spottiness (temperature disturbances) may play important role in hypersonic boundary-layer receptivity. Mechanism of the boundary-layer mode excitation by vorticity/entropy waves is discussed in Section 5.

(iv) Transition process is described by the initial boundary value problem, which requires distributions of the normal mode amplitudes at the instability growth onset. These initial data are determined from receptivity analyses comprising the identification of external disturbances, the determination of the most sensitive regions, and prediction of the normal mode propagation from these regions to the instability growth onset. All these steps relate to the disturbance field in the region located *upstream* from the lower neutral branch. However, previous studies have been focused on stability analysis related to the *downstream* region only. In this report, we show that the disturbance pre-history of hypersonic boundary

layer is more complicated than in the moderate supersonic case due to the presence of the disturbance spectrum singularities.

(v) Recent experimental studies [36] relevant to the non-linear phase of supersonic flat-plate transition showed that boundary-layer disturbances of discrete spectrum are able to generate intensive acoustic waves of continuous spectrum. Release of the boundary-layer disturbance energy to the external flow can affect the transition onset process. This mechanism seems to be stronger at higher Mach numbers. Since the PSE analysis does not account for the continuous spectrum disturbances, these effects cannot be predicted using the PSE code. Similar comment can be made regarding receptivity problem coupling external disturbance of continuous spectrum with the boundary-layer modes of discrete spectrum. To capture these mechanisms, the PSE method should be modified or combined with alternative methods.

These examples show that the extension of subsonic and low supersonic stability concepts and transition prediction methodology to hypersonic speeds is not a trivial problem. Hypersonic boundary layer receptivity, instability and non-linear mechanisms reveal new features which should be studied independently. A multiple-mode method rather than a single-mode approach can help to explain mentioned above singular features of hypersonic transition. This method can be able to evaluate receptivity of hypersonic boundary layers and provide initial data for the PSE calculations. That will help to realize the amplitude method for the hypersonic transition prediction.

This report addresses the initial phase of the hypersonic boundary-layer transition comprising excitation of unstable normal modes (receptivity problem) and their downstream evolution from receptivity regions to the instability growth onset (instability pre-history problem). In Section 2, we formulate basic formalism of the multiple-mode method following to previous studies relevant to subsonic and moderate supersonic speeds [12], [37], [38]. In Section 3, we analyze the spectrum topology for hypersonic boundary layer

including the continuous spectrum. Then we consider normal mode characteristics of the hypersonic boundary layer on a sharp cone and identify singular regions relevant to synchronism between normal modes and external acoustic waves, synchronism between the first mode and external vorticity/entropy waves, and synchronism between the first and second modes. In Section 4, we study coupling between the first and second mode in correspondent synchronism region and establish the inter-mode exchange rule. In Section 5, we consider synchronism between the boundary-layer modes and the entropy/vorticity waves and estimate receptivity to the freestream turbulence and entropy spottiness. In Section 6, we summarize results, formulate possible scenarios for the initial phase of hypersonic transition in conical and planar boundary layers, and discuss their consistency with experimental evidences.

2. Basic formalism

In this section, we describe the basic formalism of the multiple-mode method, which provides coupling between external disturbances and boundary-layer normal modes (receptivity problem) as well as coupling between different normal modes (inter-mode exchange problem). In the framework of linear stability theory, receptivity and inter-mode exchange mechanisms are due to non-parallel effects of basic flow. The multiple-mode analysis is based on the following formalism developed in [12], [37]-[39].

We consider a two-dimensional boundary layer mean flow with the velocity components $(U,V)=(U^*,V^*)/U_e^*$, pressure $P=P^*/(\rho_e^* U_e^{*2})$ and temperature $T=T^*/T_e^*$. Due to downstream growth of the boundary layer thickness, the mean flow profiles are functions of the longitudinal coordinate $x=x^*/L^*$, *i.e.*

$$U=U(x,y),\ V=\varepsilon\tilde{V}(x,y),\ P=P(x),\ T=T(x,y) \tag{2.1}$$

where $y = y^* / \delta$ is coordinate normal to the wall surface , $\delta = \sqrt{\nu_e^* L^* / U_e^*}$ is boundary layer scale, and L^* is typical streamwise distance from the body nose to the flow region to be analyzed. In many cases, this distance is associated with the lower neutral branch locus.

Unsteady disturbance field is represented as a vector

$$\vec{\Psi}(x,y,t) = (u,\ \frac{\partial u}{\partial y},\ v,\ p,\ \theta,\ \frac{\partial \theta}{\partial y},\ \frac{\partial u}{\partial x},\ \frac{\partial v}{\partial x},\ \frac{\partial \theta}{\partial x})^T \tag{2.2}$$

where $t = t^* U_e^* / \delta$ is time; u and v are streamwise and vertical velocity components; p is pressure and θ is temperature. For harmonic disturbances of a given angular frequency $\omega = \omega^* \delta / U_e^*$ and small amplitude τ, the disturbance vector is expressed in the form

$$\vec{\Psi} = \tau \vec{A}(x,y)\exp(-i\omega t) \tag{2.3}$$

The disturbance amplitude $\vec{A}$ is a solution of linearized Navier-Stokes equations, which can be written in the matrix-operator form

$$H_0 \vec{A} + \varepsilon H_2 \frac{\partial \vec{A}}{\partial x} = 0 \tag{2.4}$$

where the operator H_0 is expressed as

$$H_0 = \frac{\partial}{\partial y} L_0 \frac{\partial}{\partial y} + L_1 \frac{\partial}{\partial y} - H_1 - \varepsilon H_3$$

Elements of the 9x9 matrices L_0, L_1, H_1, H_2 and H_3 are functions on mean flow characteristics. Their explicit form is given in [12] and [38]. Elements of the matrix H_3 are

proportional to terms $\frac{\partial U}{\partial x}$, $\frac{\partial T}{\partial x}$, $\tilde{V}$ and $\frac{\partial \tilde{V}}{\partial y}$. Small parameter $\varepsilon = 1/R_L$ characterizes non-parallel effects, where the Reynolds number is $R_L = \sqrt{U_e^* L^* / \nu_e^*}$. If the disturbance amplitude is identified in a certain cross-section $x = x_0$ and disturbances satisfy no-slip conditions on the wall, then the boundary conditions are

$$\vec{A}(x_0, y) = \vec{A}_0(y) \tag{2.5a}$$

$$A_1(x,0) = A_3(x,0) = A_5(x,0) = 0 \tag{2.5b}$$

$$|\vec{A}(x,y)| < \infty,\ y \to \infty \tag{2.5c}$$

Solution of Eq. (2.4) with the boundary conditions (2.5) can be represented as an expansion in an eigenvector system of the locally homogeneous problem

$$\frac{\partial}{\partial y}\left(L_0 \frac{\partial \vec{A}}{\partial y}\right) + L_1 \frac{\partial \vec{A}}{\partial y} = H_1 \vec{A} + \varepsilon H_2 \frac{\partial \vec{A}}{\partial x} \tag{2.6a}$$

$$A_1(x,0) = A_3(x,0) = A_5(x,0) = 0 \tag{2.6b}$$

$$|\vec{A}(x,y)| < \infty,\ y \to \infty \tag{2.6c}$$

The biorthogonal eigenvector system $\{\vec{A}_\alpha(x,y), \vec{B}_\alpha(x,y)\}$ is defined as a family of solutions for the following problems [38], [39]:

Direct problem:

$$\frac{\partial}{\partial y}\left(L_0 \frac{\partial \vec{A}_\alpha}{\partial y}\right) + L_1 \frac{\partial \vec{A}_\alpha}{\partial y} = H_1 \vec{A}_\alpha + i\alpha H_2 \vec{A}_\alpha \tag{2.7a}$$

$$A_{\alpha 1}(x,0) = A_{\alpha 3}(x,0) = A_{\alpha 5}(x,0) = 0 \tag{2.7b}$$

$$|\vec{A}_\alpha(x,y)| < \infty,\ y \to \infty \tag{2.7c}$$

Adjoint problem:

$$\frac{\partial}{\partial y}\left(L_0^*\frac{\partial \vec{B}_\alpha}{\partial y}\right) - L_1^*\frac{\partial \vec{B}_\alpha}{\partial y} = H_1^*\vec{B}_\alpha - i\overline{\alpha}H_2^*\vec{B}_\alpha \tag{2.8a}$$

$$B_{\alpha 2}(x,0) = B_{\alpha 4}(x,0) = B_{\alpha 6}(x,0) = 0 \tag{2.8b}$$

$$|\vec{B}_\alpha(x,y)| < \infty,\ y \to \infty \tag{2.8c}$$

Here asterisk denotes a conjugate matrix and upper bar denotes complex conjugate values. Eigenfunction $\vec{A}_\alpha(x,y)$ characterizes an amplitude distribution of the elementary wave

$$\vec{A}_\alpha(x,y)\exp[\varphi_\alpha(x) - i\omega t],\ \ \varphi_\alpha(x) = i\varepsilon^{-1}\int_{x_0}^{x}\alpha(x)dx \tag{2.9}$$

The eigenvectors satisfy the following orthogonality conditions

$$\left\langle H_2\vec{A}_\alpha, \vec{B}_\beta \right\rangle = \Delta_{\alpha\beta} \tag{2.10}$$

where the scalar product is defined as

$$\left\langle \vec{A}, \vec{B} \right\rangle = \lim_{\kappa \to 0}\int_0^\infty e^{-\kappa y}(\vec{A}, \vec{B})dy,\ \ (\vec{A}, \vec{B}) = \sum_{j=1}^{9} A_j\overline{B}_j,\ \ \kappa > 0 \tag{2.11}$$

Here $\Delta_{\alpha\beta}$ is Kronecker symbol, if one of the eigenvalues α, β belongs to the discrete spectrum; $\Delta_{\alpha\beta} = \delta(\alpha - \beta)$ is delta-function, if both eigenvalues belong to the continuous spectrum.

Solution of the problem (2.4), (2.5) is represented as the eigenmode decomposition

$$\vec{A} = \sum_{\alpha} c_{\alpha}(x)\vec{A}_{\alpha}(x,y)\exp[\varphi_{\alpha}(x)] \tag{2.12}$$

where $\sum_{\alpha}$ denotes summation over discrete spectrum and integration over continuous spectrum. Substituting (2.12) into Eq. (2.4), multiplying by $\vec{B}_{\beta}$ and accounting for the orthogonality condition (2.10), we obtain the ordinary differential equation system for the amplitude coefficients $c_{\alpha}(x)$

$$\frac{dc_{\alpha}}{dx} = \sum_{\beta} c_{\beta}(x)W_{\alpha\beta}(x)\exp[\varphi_{\beta} - \varphi_{\alpha}] \tag{2.13}$$

$$c_{\alpha} = \left\langle H_2\vec{A}_0, \vec{B}_{\alpha} \right\rangle \text{ at } x = x_0$$

where matrix elements are determined as

$$W_{\alpha\beta} = -\left\langle H_2\frac{\partial\vec{A}_{\beta}}{\partial x}, \vec{B}_{\alpha} \right\rangle - \left\langle H_3\vec{A}_{\beta}, \vec{B}_{\alpha} \right\rangle \tag{2.14}$$

For an arbitrary normalization of the eigenfunctions $\vec{A}_{\alpha}, \vec{B}_{\alpha}$, these matrix elements are expressed as

$$W_{\alpha\beta} = -\frac{\left\langle H_2\frac{\partial\vec{A}_{\beta}}{\partial x}, \vec{B}_{\alpha} \right\rangle + \left\langle H_3\vec{A}_{\beta}, \vec{B}_{\alpha} \right\rangle}{\left\langle H_2\vec{A}_{\alpha}, \vec{B}_{\alpha} \right\rangle} \tag{2.15}$$

Diagonal elements $W_{\alpha\alpha}$ relate to a single mode evolution in the non-parallel boundary layer. Non-parallel stability analyses [12], [41] and the PSE method [19], [20] address this case.

Non-diagonal elements $W_{\alpha\beta}$ are responsible for exchange between modes with eigenvalues α and β. If one of these modes belongs to the continuous spectrum, then the elements $W_{\alpha\beta}$ provide coupling between external disturbances and the boundary-layer modes (receptivity problem). If both modes belong to the discrete spectrum, these elements are responsible for the exchange between normal modes (the inter-mode exchange problem). If the mean flow is parallel, then all matrix elements $W_{\alpha\beta} = 0$, and no coupling between modes.

In the framework of this formalism, the receptivity analysis and the inter-mode exchange analysis comprises the following steps:

- Identify the biorthogonal eigenvector system $\{\vec{A}_\alpha(x,y), \vec{B}_\alpha(x,y)\}$ including discrete and continuous spectrums of $\alpha(x,\omega)$.
- Specify initial conditions at $x = x_0$.
- Simplify the equation system (2.13) neglecting eigenmodes, which are not important for particular problem (cutoff procedure).
- Calculate eigenvalues, eigenfunctions and matrix elements (2.14).
- Solve the cutoff equation system for the amplitude coefficients $c_\alpha(x)$.

3. Disturbance spectrum

Analysis

The local homogeneous problem (2.7) can be reduced to the well known linear stability problem [12], [38], [39]

$$\frac{d\vec{z}_\alpha}{dy} = G_0\vec{z}_\alpha \tag{3.1a}$$

$$z_{\alpha 1} = z_{\alpha 3} = z_{\alpha 5} = 0,\ y = 0 \tag{3.1b}$$

$$|\vec{z}_\alpha| < \infty,\ y \to \infty \tag{3.1c}$$

where $\vec{z}_\alpha = (A_{\alpha 1}, A_{\alpha 2}, A_{\alpha 3}, A_{\alpha 4}, A_{\alpha 5}, A_{\alpha 6})^T$, and G_0 is 6×6 matrix depending on basic flow characteristics, frequency ω, eigenvalue α, and Reynolds number $R = \sqrt{U_e^* x^* / \nu_e^*}$. Its non-zero elements are given in [41]. System (3.1) has six independent solutions $\vec{q}_1, \vec{q}_2, \ldots, \vec{q}_6$ with the following asymptotic forms

$$\vec{q}_j \to \vec{q}_j^{(0)} e^{\lambda_j y} \text{ at } y \to \infty,\ j = 1,\ldots,6 \tag{3.2}$$

where λ_j are solutions of the characteristic equation

$$\det\|G_0 - \lambda E\| = 0 \text{ as } y \to \infty \tag{3.3}$$

Eq. (3.3) can be written in the explicit form

$$(b_{11} - \lambda^2)[(b_{22} - \lambda^2)(b_{33} - \lambda^2) - b_{23}b_{32}] = 0\ , \tag{3.4}$$

$$b_{11} = G_0^{21},\ b_{22} = G_0^{42}G_0^{24} + G_0^{43}G_0^{34} + G_0^{46}G_0^{64},$$

$$b_{23} = G_0^{42}G_0^{25} + G_0^{43}G_0^{35} + G_0^{46}G_0^{65},$$

$$b_{32} = G_0^{64},\ b_{33} = G_0^{65}$$

Eq. (3.4) has the following solutions

$$\lambda_1^2 = b_{11},\ \lambda_{2,3}^2 = \frac{b_{22} + b_{33}}{2} \mp \frac{1}{2}\sqrt{(b_{22} - b_{33})^2 - 4b_{23}b_{32}} \tag{3.5}$$

Specifying branches as $\mathrm{Re}(\lambda_1, \lambda_2, \lambda_3) < 0$, we can express the asymptotic forms (3.2) as

$$\vec{q}_{1,2} \to \vec{q}_{1,2}^{(0)} e^{\pm\lambda_1 y},\ \vec{q}_{3,4} \to \vec{q}_{3,4}^{(0)} e^{\pm\lambda_2 y},\ \vec{q}_{5,6} \to \vec{q}_{5,6}^{(0)} e^{\pm\lambda_3 y} \text{ at } y \to \infty \tag{3.6}$$

If $\mathrm{Re}(\lambda_j) \neq 0$ for all $j = 1, 2, 3$, then solution of the problem (3.1) is the linear decomposition of three vectors

$$\vec{z}_\alpha = C_1\vec{q}_1 + C_3\vec{q}_3 + C_5\vec{q}_5 \tag{3.7}$$

where constants C_1, C_3 and C_5 are determined from the wall boundary condition (3.1b)

$$\begin{aligned} C_1 q_{11} + C_3 q_{13} + C_5 q_{15} &= 0 \\ C_1 q_{31} + C_3 q_{33} + C_5 q_{35} &= 0 \\ C_1 q_{51} + C_3 q_{53} + C_5 q_{55} &= 0 \end{aligned} \tag{3.8}$$

Equation system (3.8) has non-trivial solutions, if its determinant is zero; *i.e.*

$$\det \begin{Vmatrix} q_{11} & q_{13} & q_{15} \\ q_{31} & q_{33} & q_{35} \\ q_{51} & q_{53} & q_{55} \end{Vmatrix} = 0 \tag{3.9}$$

The dispersion relationship (3.9) gives a discrete spectrum $\alpha_n(\omega, x)$ related to the boundary layer normal modes.

If one of the eigenvalues λ_j has zero real part, $\mathrm{Re}(\lambda_j) = 0$, then solution of the problem (3.1) is a linear decomposition of four vectors and describes waves of continuous spectrum. Analysis [39] shows that supersonic boundary layer has seven branches of continuous spectrum: three branches correspond to waves propagating upstream, two branches correspond to acoustic waves propagating downstream and two branches correspond to vorticity and entropy waves propagating downstream. The continuous spectrum branches and discrete eigenvalues are schematically shown in Fig. 1. Further analysis addresses the

continuous spectrum waves propagating downstream only. Their eigenvalues belong to the upper half of complex α -plane.

If $\lambda_1^2 = -k^2$ and $k > 0$ is real parameter, then the wavenumber $\alpha_v(\omega, k)$ corresponds to vorticity waves of the amplitude

$$\vec{z}_\alpha = C_1\vec{q}_1 + C_2\vec{q}_2 + C_3\vec{q}_3 + C_5\vec{q}_5 \tag{3.11}$$

which has the asymptotic form

$$\vec{z}_v = C_1\vec{q}_1^{(0)}e^{iky} + C_2\vec{q}_2^{(0)}e^{-iky} + C_3\vec{q}_3^{(0)}e^{\lambda_2 y} + C_5\vec{q}_5^{(0)}e^{\lambda_3 y} \text{ at } y \to \infty \tag{3.12}$$

For large Reynolds numbers $R = \sqrt{U_e^* x^* / \nu_e^*} \equiv R_L\sqrt{x}$, the vorticity wavenumber is approximated as

$$\alpha_v = \omega + i\frac{k^2 + \omega^2}{R} + O(R^{-2}) \tag{3.13}$$

If $\lambda_2^2 = -k^2$ and $k > 0$, then the wavenumber $\alpha_e(\omega, k)$ corresponds to entropy waves of the amplitude

$$\vec{z}_e = C_1\vec{q}_1 + C_3\vec{q}_3 + C_4\vec{q}_4 + C_5\vec{q}_5 \tag{3.14}$$

which has the asymptotic form

$$\vec{z}_e = C_1\vec{q}_1^{(0)}e^{\lambda_1 y} + C_3\vec{q}_3^{(0)}e^{iky} + C_4\vec{q}_4^{(0)}e^{-iky} + C_5\vec{q}_5^{(0)}e^{\lambda_3 y} \text{ at } y \to \infty \tag{3.15}$$

The entropy wavenumber is approximated as

$$\alpha_e = \omega + i\frac{k^2+\omega^2}{\sigma R} + O(R^{-2}) \tag{3.16}$$

where σ is Prandtl number. According to Eqs. (3.13) and (3.16) vorticity and entropy waves propagate downstream with the phase speed $c_r \equiv \omega / \alpha_r = 1 + O(R^{-2})$, and slowly dissipate due to viscosity.

Equation, $\lambda_3^2 = -k^2$ at $k > 0$, gives three branches. Two of them correspond to acoustic waves of the wavenumber $\alpha_a(\omega, k)$ propagating downstream in a supersonic flow. Their amplitude

$$\vec{z}_e = C_1\vec{q}_1 + C_3\vec{q}_3 + C_5\vec{q}_5 + C_6\vec{q}_6 \tag{3.17}$$

has the asymptotic form

$$\vec{z}_a = C_1\vec{q}_1^{(0)}e^{\lambda_1 y} + C_3\vec{q}_3^{(0)}e^{\lambda_2 y} + C_5\vec{q}_5^{(0)}e^{iky} + C_6\vec{q}_6^{(0)}e^{-iky} \text{ at } y \to \infty \tag{3.18}$$

For the Mach number $M_e > 1$ and $k << R$, acoustic waves are almost neutral. Their wavenumbers belong to the regions

$$\mathrm{Re}(\alpha_{a1}) \le \frac{M_e\omega}{1+M_e} + O(R^{-1}); \ \mathrm{Re}(\alpha_{a2}) \ge \frac{M_e\omega}{1-M_e} + O(R^{-1}) \tag{3.19}$$

As k increases, their decrement $\mathrm{Im}(\alpha_a)$ grows. When the parameter k is of the order of the Reynolds number R, acoustic waves transform into pressure waves, which rapidly dissipate downstream (see Fig. 1).

Numerical results

Two-dimensional boundary-layer profiles were calculated using self-similar solutions of the boundary-layer equations in the local similarity approximation [42]. The conical mean flow characteristics were obtained using the Mangler transformation according to which the flat-plate boundary-layer thickness δ_p is larger than the conical boundary-layer thickness δ_c by $\sqrt{3}$. In all calculations, it is assumed that the fluid is a perfect gas with a constant specific heats ratio $\gamma = 1.4$ and Prandtl number $\sigma = 0.72$. The viscosity temperature dependency is approximated by Sutherland's law

$$\mu(T) = \frac{(1+S)}{(T+S)} T^{3/2}$$

where $S = 110 / T_e^*$ for air temperature measured in degrees Kelvin; $\mu = \mu^* / \mu_e^*$ is nondimensional viscosity. Mean flow calculations were performed for the conditions related to the AEDC Tunnel B stability experiments on a 7 degree half angle sharp cone at zero angle of attack [25]. Comparison between theoretical and experimental distributions $\delta_c(x)$ are shown in Fig. 2 for the local Mach number $M_e = 6.8$, local temperature $T_e = 70.26$ K; the cone surface temperature is $T_w = T_{ad}$ (the insulated wall condition). It is seen that the local self-similar solution well correlates experimental data. Consequently, the viscous-inviscid interaction and the non-uniform distribution of the surface temperature near the cone tip can be neglected in this case.

Integration of the stability equations (3.1) is performed using the numerical procedure similar to that developed by Mack [21]. The analytic external solutions (3.7) provide the initial conditions for the linearly-independent solutions at the upper boundary $\eta = \eta_e$, where $\eta = y / \sqrt{x}$ is self-similar boundary-layer variable. The system (3.1) is integrated from the upper boundary η_e to the wall surface $\eta = 0$ using the fourth-order Runge-Kutta method

and the orthogonalization procedure. The eigenvalue search is performed by the Newton iteration method. Calculations are conducted for the planar boundary layer. These results have been adjusted by $\sqrt{3}$ for the comparison with the conical boundary-layer stability data [25]. That is, the eigenvalues α and the Reynolds number R have been increased by $\sqrt{3}$.

Eigenmode characteristics and boundaries of continues spectrum are shown in Figures 3a and 3b for the local Mach number $M_e = 6.8$, local temperature $T_e = 70.26$ K, the cone surface temperature $T_w = T_{ad}$, and frequency parameter $F = 10^{-4}$. These parameters correspond to stability measurements [25] performed in the AEDC Tunnel B on a 7 degree half angle sharp cone at zero angle of attack. The first and second mode eigenvalues tend to the lower and upper boundaries of acoustic spectrum respectively, when the Reynolds number is $R < 800$ (Region 1 in Fig. 3a). Asymptotic analysis [32] and numerical calculations conducted in a wide range of Mach numbers and wall temperatures showed that this upstream asymptotic behavior is typical for hypersonic boundary layers and can be used for classification of normal modes. We will call the normal mode with the phase speed $c_r \to 1+1/M_e$ at $x \to 0$ as *the first mode*, and the normal mode with the phase speed $c_r \to 1-1/M_e$ at $x \to 0$ as *the second mode*. Note that this classification is different from the Mack's classification. To avoid misunderstanding we will call the first/second mode of Mack's classification as the Mack's first/second mode.

Analysis [32] showed that synchronization of the first and second mode waves with acoustic waves of the phase speed $c_r = 1 \pm 1/M_e$ can cause a strong excitation of instability near the nose region. In conventional wind tunnels, sound is generated by vortices propagating downstream in the turbulent boundary layer on the nozzle and test section walls. Since acoustic waves from these moving sources have the phase speed $c < 1-1/M_e$, they do not satisfy the synchronism conditions. However, their interaction with the nose tip induces a local source, which generates "dangerous" disturbances of the phase speed $c = 1 \pm 1/M_e$, as schematically shown in Fig. 4. For a planar configuration (flat plate or hollow cylinder), this

local source has cylindrical shape. For the conical flow, it is concentrated near the cone tip. Since the point source on the cone tip is weaker than the line source on a plate leading edge and downstream attenuation of acoustic waves from the point source is stronger than that from a line source, receptivity of a planar configuration to acoustic disturbances should be higher than that of a conical configuration. These arguments are consistent with experimental observations [33].

Near the point $R \approx 1515$ (Region 2 in Fig. 3a) the first mode is synchronized with vorticity and entropy waves of the phase speed $c_r = 1$. In this region, the freestream vorticity and entropy disturbances may effectively generate the first mode and conversely the first mode may induce the vorticity and entropy disturbances. These mechanisms are discussed in Section 5. The first mode mass flux distribution $Q_1(y,R)$ is shown in Fig. 5. Near the synchronism point, $R \approx 1515$, oscillating "tail" indicates that the first mode penetrates outside the boundary layer. This feature can be exploited to identify the synchronism region 2 by measuring correlation between hot-wire signals inside and outside the boundary layer.

In the vicinity of the point $R \approx 1750$ (Region 3 in Fig. 3a), phase speeds of the first and second modes are very close to each other. As will be shown in Section 4, the discrete spectrum has two branch points in this region. Near the branch points a strong exchange between the boundary-layer modes can be caused by the mean flow nonparallel effect. Mechanism of this exchange will be discussed in Section 4. The synchronism is associated with local maximum of the first-mode mass flux distribution shown in Fig. 5.

The spectrum topology may be different from that shown in Figures 3a and 3b. As an example, Figures 6a and 6b illustrate the eigenvalue behavior for the local Mach number $M_e = 5.5$, wall temperature ratio $T_w / T_{ad} = 0.1$ and disturbance frequency $F = 10^{-4}$. Downstream the branch point, $R_{b1} \approx 3600$ (Region 3), the first mode gets unstable whereas

the second mode gets more stable. In Section 4, we study the spectrum behavior near the branch points and discuss cases corresponding to jumps from one topology to another.

4. Coupling between the first and second modes

Analysis

Figures 3a and 6a show that phase speeds of the first and second modes are very close to each other in the synchronism region 3. The disturbance spectrum topology in this region has been studied by Guschin and Fedorov [30], [31]. It was found that a qualitative local behavior of eigenvalues is described by the following simple dispersion relation

$$(\overline{\alpha} - a_1\overline{\omega})(\overline{\alpha} - a_2\overline{\omega}) = a_0 \tag{4.1}$$

where $\overline{\alpha} = \alpha - \alpha_0$ and $\overline{\omega} = \omega - \omega_0 = F(R - R_0)$ is local eigenvalue and angular frequency respectively; a_0, a_1 and a_2 are constants. The eigenvalues $\overline{\alpha}_{1,2}(\overline{R})$ of a given frequency F are schematically shown in Fig. 7 for the case of $a_0<0$, $a_1>a_2>0$. Solution of Eq. (4.1) has two branches

$$\overline{\alpha}_{1,2} = \frac{a_1 + a_2}{2} F\overline{R} \mp \sqrt{\frac{1}{4}(a_1 - a_2)^2 F^2 \overline{R}^2 + a_0} \tag{4.2}$$

The branch points are defined as

$$\overline{R}_{b1,2} = \mp \frac{2\sqrt{|a_0|}}{F(a_1 - a_2)} \tag{4.3}$$

They are located on the real axis of complex $\overline{R}$-plane. If the branch points are bypassed

from the upper side as shown in Fig. 7, then the first mode is stable, $\mathrm{Im}(\overline{\alpha}_1) > 0$, and the second mode is unstable, $\mathrm{Im}(\overline{\alpha}_2) < 0$, in the region $\overline{R}_{b1} < \overline{R} < \overline{R}_{b2}$. This spectrum topology is consistent with the numerical result illustrated by Figures 3a and 3b. As will be shown below, the branch point R_{b1} is slightly shifted below the real axis of the complex R-plane due to viscous effects. As the Reynolds number increases along the real axis, this branch point is bypassed from the upper side similar to the case shown in Fig. 7. Figures 6a and 6b illustrate another case when the branch point R_{b1} is shifted to the upper half of the complex R-plane and bypassed from the lower side. The first-mode wave gets unstable downstream from the branch point R_{b1}, whereas the second mode gets stable.

Now we consider disturbance behavior near the branch point $x_{b1} = (R_{b1} / R_L)^2$. Eigenvalues of the first and second modes can be approximated as

$$\alpha_{1,2} = \alpha_0 \pm \Lambda\sqrt{X} + \ldots \tag{4.4}$$

where $X = x - x_{b1}$ is local variable. Using the basic formalism of Section 3, we can describe the coupling between the first and second mode in the two-mode approximation. *I.e.* solution of Eq. (2.4) is approximated as

$$\vec{A} = c_1(x)\vec{A}_1(x,y)\exp[\varphi_1(x)] + c_2(x)\vec{A}_2(x,y)\exp[\varphi_2(x)] \tag{4.5}$$

$$\varphi_{1,2} = i\varepsilon^{-1}\int_{x_{b1}}^{x} \alpha_{1,2}(x)dx \tag{4.6}$$

where the eigenfunctions $\vec{A}_{1,2}$ are solutions of the homogeneous problem

$$(H_0 + i\alpha H_2)\vec{A}_j = 0 \tag{4.7a}$$

$$A_{j1}(x,0) = A_{j3}(x,0) = A_{j5}(x,0) = 0 \tag{4.7b}$$

$$|\vec{A}_j(x,y)| \to 0,\ y \to \infty;\ j = 1,2 \tag{4.7c}$$

The amplitude coefficients $c_{1,2}$ are solutions of the ordinary differential equation system

$$\frac{dc_1}{dx} = c_1 W_{11} + c_2 W_{12} \exp(\varphi_2 - \varphi_1) \tag{4.8a}$$

$$\frac{dc_2}{dx} = c_2 W_{22} + c_1 W_{21} \exp(\varphi_1 - \varphi_2) \tag{4.8b}$$

where the matrix elements are defined as

$$W_{jk} = -\frac{\left\langle H_2 \frac{\partial \vec{A}_k}{\partial x}, \vec{B}_j \right\rangle}{\left\langle H_2 \vec{A}_j, \vec{B}_j \right\rangle};\ j = 1,2;\ k = 1,2 \tag{4.8c}$$

In the vicinity of the branch point, $X = 0$, the operators H_0, H_2 and eigenfunctions $\vec{A}_{1,2}$ are expanded in the following series

$$H_0 = H_{00} + XH_{01} + \ldots \tag{4.9a}$$

$$H_2 = H_{20} + XH_{21} + \ldots \tag{4.9b}$$

$$\vec{A}_j = \vec{A}^{(0)} + (\alpha_j - \alpha_0)\vec{A}^{(1)} + \ldots;\ j = 1,2 \tag{4.9c}$$

Substituting (4.4) and (4.9) into Eqs. (4.7) we obtain the following problems

$$(H_{00} + i\alpha_0 H_{20})\vec{A}^{(0)} = 0 \tag{4.10a}$$

$$A_1^{(0)}(x,0) = A_3^{(0)}(x,0) = A_5^{(0)}(x,0) = 0 \tag{4.10b}$$

$$|\vec{A}^{(0)}(x,y)| \to 0,\ y \to \infty \tag{4.10c}$$

$$(H_{00} + i\alpha_0 H_{20})\vec{A}^{(1)} = -iH_{20}\vec{A}^{(0)} \tag{4.11a}$$

$$A_1^{(1)}(x,0) = A_3^{(1)}(x,0) = A_5^{(1)}(x,0) = 0 \tag{4.11b}$$

$$|\vec{A}^{(1)}(x,y)| \to 0,\ y \to \infty \tag{4.11c}$$

$$(H_{00} + i\alpha_0 H_{20})\vec{A}^{(2)} = -\Lambda^2 H_{20}\vec{A}^{(1)} - (H_{01} + i\alpha_0 H_{21})\vec{A}^{(0)} \tag{4.12a}$$

$$A_1^{(2)}(x,0) = A_3^{(2)}(x,0) = A_5^{(2)}(x,0) = 0 \tag{4.12b}$$

$$|\vec{A}^{(2)}(x,y)| \to 0,\ y \to \infty \tag{4.12c}$$

A non-trivial solution of the problems (4.11) and (4.12) exists, when the right-hand side of Eqs. (4.11a) and (4.12a) is orthogonal to the adjoint problem solution $\vec{B}^{(0)}$; *i.e.*

$$\left\langle H_{20}\vec{A}^{(0)}, \vec{B}^{(0)} \right\rangle = 0 \tag{4.13}$$

$$i\Lambda^2 \left\langle H_{20}\vec{A}^{(1)}, \vec{B}^{(0)} \right\rangle + \left\langle (H_{01} + i\alpha_0 H_{21})\vec{A}^{(0)}, \vec{B}^{(0)} \right\rangle = 0 \tag{4.14}$$

Eq. (4.13) can be used for the branch point search. In turn, the constant Λ can be determined from Eq. (4.14).

Similar expansions can be made for the adjoint problem solution $\vec{B}$. Substituting them into Eq. (4.8c) we obtain the following form of the matrix elements

$$W_{jk} = \frac{(-1)^{j+k-1}}{4X}\ ;\ j = 1, 2\ ;\ k = 1, 2 \tag{4.15}$$

In the inner region with the variable $\xi = \varepsilon^{-2/3} X = O(1)$, the equation system (4.8) is written as

$$\frac{dc_1}{d\xi} = \frac{1}{4\xi}\left[-c_1 + c_2 \exp\left(-\frac{4}{3} i\Lambda\lambda\xi^{3/2}\right)\right] \tag{4.16a}$$

$$\frac{dc_2}{d\xi} = \frac{1}{4\xi}\left[c_1 \exp\left(\frac{4}{3} i\Lambda\lambda\xi^{3/2}\right) - c_2\right] \tag{4.16b}$$

Since this system does not depend on the mean flow profiles, its solution can be used to model the inter-mode exchange for broad class of shear layers with the eigenvalue behavior similar to that given by Eq. (4.4). Equations (4.16) can be reduced to the Airy equation using the following transformation

$$f(\xi) = c_1(\xi)\exp(\Delta(\xi)) + c_2(\xi)\exp(-\Delta(\xi)) \tag{4.17a}$$

$$\Delta(\xi) = \frac{2}{3} i\Lambda\xi^{3/2} \tag{4.17b}$$

Substituting (4.17) into (4.16) we obtain

$$\frac{d^2 f}{d\xi^2} + \Lambda^2 \xi = 0 \tag{4.18}$$

Similar equation has been derived by Fedorov and Khokhlov [32] using an alternative asymptotic analysis of Eq. (2.4).

Asymptotic behavior of the Airy equation solution at $|\xi| \to \infty$ depends on the orientation of Stokes lines l_j, $j = 1, 2, 3$, which are defined by the equation $\mathrm{Re}[\Delta(\xi)] = 0$ in the complex ξ-plane. We consider the Stokes lines topology schematically shown in Fig. 8. This

topology corresponds to the case, when the first and second modes are almost neutral in the upstream region $\xi < 0$. Downstream from the branch point one of these modes gets essentially unstable and another gets stable. Numerical examples of such spectrum splitting are shown in Figures 3a, 3b and 6a, 6b.

Following to the analysis of Fedoruk [43] we introduce the canonical domains

$$D_j : l_j \in D_j, l_{k\neq j} \in \partial D_j$$

and specify branches of the function $\Delta(\xi)$ so that $\mathrm{Im}(\Delta) > 0$ at $\xi \in l_j \in D_j$. Then the real part $\mathrm{Re}(\Delta)$ is positive to the right of the Stokes line l_j, and it is negative to the left of the Stokes line l_j. Solution of the Airy equation (4.18) has the asymptotic form

$$f \to S_j \xi^{-1/4} [a_j \exp(\Delta) + b_j \exp(-\Delta)], \quad |\xi| \to \infty \tag{4.19}$$

where $\xi \in D_j$; constants S_j satisfy the following conditions

$$|S_j| = 1, \text{ and } \arg\left(S_j \xi^{-1/4}\right) = 0 \text{ at } \xi \in l_j; \; j = 1, 2, 3$$

Constants a_j and b_j are coupled by the relations [43]

$$\begin{bmatrix} a_{j+1} \\ b_{j+1} \end{bmatrix} = \exp(-i\pi/6) \begin{bmatrix} 0 & 1 \\ 1 & i \end{bmatrix} \begin{bmatrix} a_j \\ b_j \end{bmatrix} \text{ at } j = 1, 2 \tag{4.20a}$$

$$\begin{bmatrix} a_1 \\ b_1 \end{bmatrix} = \exp(-i\pi/6) \begin{bmatrix} 0 & 1 \\ 1 & i \end{bmatrix} \begin{bmatrix} a_3 \\ b_3 \end{bmatrix} \tag{4.20b}$$

Eqs. (4.20) determine the exchange between the first and second modes as the longitudinal coordinate x passes through the interaction region $|x - x_{b1}| = O(\varepsilon^{2/3})$ and intersects one of the Stokes lines. Since the transition matrix has a universal form, Eq. (4.20) establishes the inter-mode exchange rule for various weakly nonparallel mean flows, which have similar topology of the discrete spectrum. This rule can be expressed in more generic form as

$$\begin{bmatrix} A^{+}_{stable} \\ A^{+}_{unstable} \end{bmatrix} = \exp(-i\frac{\pi}{6}) \cdot \begin{bmatrix} 0 & 1 \\ 1 & i \end{bmatrix} \cdot \begin{bmatrix} A^{-}_{stable} \\ A^{-}_{unstable} \end{bmatrix} \tag{4.21}$$

where (A^{-}_{stable}, $A^{-}_{unstable}$) and (A^{+}_{stable}, $A^{+}_{unstable}$) are amplitudes of stable and unstable mode upstream and downstream from the interaction region respectively. For the eigenvalues shown in Figures 3a and 3b, the amplitudes A^{-}_{stable}, A^{+}_{stable} correspond to the first mode, and the amplitudes $A^{-}_{unstable}$, $A^{+}_{unstable}$ correspond to the second mode. For the case shown in Figures 6a and 6b, the amplitudes A^{-}_{stable}, A^{+}_{stable} correspond to the second mode, and the amplitudes $A^{-}_{unstable}$, $A^{+}_{unstable}$ correspond to the first mode. The inter-mode exchange diagram shown in Fig. 9 indicates that the stable-mode wave excites the unstable-mode wave of the same amplitude, $|A^{+}_{unstable}| \approx |A^{-}_{stable}|$. In turn, the unstable mode excites the stable mode and propagates downstream with the same initial amplitude. In both cases, the unstable mode occurs in the downstream region.

In the first order approximation, the inter-mode exchange does not depend on the small parameter ε, which characterizes nonparallel effects. As ε tends to zero, the interaction region is expanded as $\varepsilon^{-2/3}$, whereas the local disturbance amplitude grows as $\varepsilon^{-1/6}$. Both trends compensate each other so that coupling between the input and output amplitudes does not change.

Numerical results

Numerical analysis of the dispersion relation (3.9) is extended to the complex values of the Reynolds number R. For self-similar approximation of the mean boundary-layer flow, this extension is trivial, because the mean flow profiles do not depend on the Reynolds number and the stability matrix G_0 from Eq. (3.1a) depends on the Reynolds number in parametrical explicit form only. In this case the eigenvalue problem (3.1) can be solved for complex values of R using the same numerical procedures as in cases of real R. The branch-point Reynolds number R_{b1} is calculated from Eq. (4.13), which can be written as

$$\left\langle H_2 \vec{A}_j, \vec{B}_j \right\rangle = 0 \text{ at } j = 1, 2 \text{ and } R = R_{b1} \tag{4.22}$$

Eq. (4.22) is solved using the Newton iteration technique. Distributions $\mathrm{Re}[R_{b1}(F)]$ and $\mathrm{Im}[R_{b1}(F)]$ are shown in Figures 10a and 10b for the case: local Mach number $M_e = 6.8$, wall temperature ratio $T_w / T_{ad} = 1$. It is seen that the branch point is located in the lower half of the complex R-plane near the real axis. Since the branch point is bypassed from the upper side, the spectrum splitting is similar to the case shown in Fig. 3a and 3b.

Figures 11 and 12 show that the real part of the branch point, $\mathrm{Re}(R_{b1})$, is close to the low branch of the second-mode neutral curve predicted by Simen and Dallmann [28]. Discrepancy between experimental data and stability calculations [28] observed near the lower neutral branch may be due to singular behavior of the disturbance field in the interaction region, $R - R_{b1} = O(R_{b1}^{1/3})$, corresponding to the slow variable range $|x - x_{b1}| = O(\varepsilon^{2/3})$. According to the asymptotic formula (4.19), the disturbance amplitude has a local maximum proportional to $\varepsilon^{-1/6}$ (see also the eigenfunction in Fig. 5). This local increase of the disturbance amplitude can be misinterpreted as the downstream growth of the boundary-layer instability. Relatively small increments calculated from experimental measurements near the lower neutral branch may relate to this effect.

Figures 13a and 13b show the branch-point Reynolds number R_{b1} as a function of local Mach number M_e at various wall temperature ratios T_w / T_{ad} for the disturbance frequency parameter $F = 10^{-4}$. For the cooled wall case, $T_w / T_{ad} = 0.1$, the imaginary part $\mathrm{Im}(R_{b1})$ changes sign at $M_{e*} \approx 5.9$. In the region, $M_e > M_{e*}$, the branch point belongs to the lower half of the complex R-plane. As the Reynolds number increases along the real axis, the branch point R_{b1} is bypassed from the upper side as schematically shown in Fig. 7. *I.e.* the second mode is stable and the first mode is unstable in the downstream region $R > \mathrm{Re}(R_{b1})$. This topology corresponds to the case shown in Fig. 14a and 14b for $M_e = 5.95$ and $T_w / T_{ad} = 0.1$. In the region $M_e < M_{e*}$, the branch point belongs to the upper half of the complex R-plane, and it is bypassed from lower side. The second mode is unstable and the first mode is stable in the downstream region $R > \mathrm{Re}(R_{b1})$. This topology corresponds to the case shown in Figures 6a and 6b for $M_e = 5.5$ and $T_w / T_{ad} = 0.1$. Comparing these cases we conclude that small change of the Mach number near the intersection point M_{e*} leads to the jump from one spectrum topology to another. However, the inter-mode exchange rule (4.21) shows that the unstable mode amplitude is approximately the same in both cases; *i.e.* the initial amplitude of instability is weakly sensitive to this jump.

If the real axis passes through the local region $|x - x_{b1}| = O(\varepsilon^{2/3})$, *i.e.* $|\mathrm{Im}(x_{b1})| = O(\varepsilon^{2/3})$ and $|\mathrm{Im}(R_{b1})| = O(\varepsilon^{-1/3})$, then the normal mode decomposition has singular behavior in the vicinity of the branch point R_{b1}. According to Eq. (4.19) the normal wave amplitude tends to infinity as $R \to R_{b1}$. Moreover, the group velocity of normal waves

$$V_g = \mathrm{Re}\left(\frac{\partial \omega}{\partial \alpha}\right) \equiv \frac{1}{\mathrm{Re}(\partial \alpha / \partial \omega)} = \frac{1}{F \partial \alpha_r / \partial R} \tag{4.23}$$

rapidly decreases to minus infinity and then jumps to plus infinity as the Reynolds number crosses the branch point from upstream to downstream region. These singularities can cause

significant difficulties in the PSE integration near the branch points of discrete spectrum. Standard stability calculations using the e^{Malik} or COSAL code can also be affected, because these codes determine the instability trajectory from the group velocity analysis.

5. Receptivity to vorticity/entropy waves

Problem formulation

In Region 2 indicated in Fig. 3a (see also Fig. 6a), the first-mode eigenvalue α_1 intersects branches of vorticity/entropy waves with the phase speed $c_r = 1$. The intersection region is shown on an enlarged scale in Figures 15a and 15b for the local Mach number $M_e = 6.8$, wall temperature ratio $T_w / T_{ad} = 1$ and disturbance frequency $F = 10^{-4}$. Figure 16 shows the spectrum topology in the complex α-plane. Since the entropy-wave branch coincides with the vorticity-wave branch as the Reynolds number $R \to \infty$, both branches can be represented in the complex α-plane as one branch cut. The first-mode eigenvalue α_1 enters into the left side of the vorticity/entropy branch cut at the Reynolds number $R = R_* - 0$ and departs from its right side at the Reynolds number $R = R_* + 0$, where $R_* \approx 1515$ is synchronism point. The eigenvalue imaginary part has the jump $\Delta(\alpha_i) \approx 0.34 \cdot 10^{-2}$, whereas its real part is smooth, *i.e.* $\alpha_{1r}(R_* - 0) = \alpha_{1r}(R_* + 0)$. Eigenfunctions of the x-component velocity, $\tilde{u}(\eta) = \mathrm{Re}[z_1(\eta)]$, are shown in Fig. 17 for various Reynolds numbers in the vicinity of synchronism point R_*. These functions are normalized by the condition $\max|\tilde{u}(\eta)| = 1$. It is seen that velocity oscillations penetrate into external flow as the Reynolds number tends to the synchronism point R_* (see also Fig. 5). The eigenfunction at $R = R_* - 0$ (Line 3 in Fig. 18) is essentially different from the eigenfunction at $R = R_* + 0$ (Line 4 in Fig. 18). This is due to the fact, that asymptotic behavior of the first vector from (3.6), $\vec{q}_1 \to \vec{q}_1^{(0)} e^{\lambda_1 y}$ at $y \to \infty$, is very sensitive to the eigenvalue jump because $\Delta\lambda_1 \approx \sqrt{iR\Delta\alpha} = O(1)$. Consequently, *the first mode should be treated as two different*

modes: one mode corresponds to the region $R < R_*$ and another to the region $R > R_*$.

We assume that nonparallel effects can cause significant interaction between the first mode and vorticity/entropy waves in the synchronism region 2 (see Figures 3a and 6a). Neglecting other modes of discrete and continuous spectrum we represent solution (2.12) in the form

$$\vec{A} = c_1(x)\vec{A}_1(x,y)\exp(\varphi_1) + \int_0^\infty c_v(x,k)\vec{A}_v(x,y;k)\exp(\varphi_v)dk +$$

$$+\int_0^\infty c_e(x,k)\vec{A}_e(x,y;k)\exp(\varphi_e)dk \qquad (5.1a)$$

$$\varphi_1(x) = i\varepsilon^{-1}\int_{x_0}^x \alpha_1(x)dx, \quad \varphi_v(x) = i\varepsilon^{-1}\int_{x_0}^x \alpha_v(x,k)dx, \quad \varphi_e(x) = i\varepsilon^{-1}\int_{x_0}^x \alpha_e(x,k)dx \qquad (5.1b)$$

where subscripts "v" and "e" denote vorticity and entropy waves respectively. The equation system (2.13) is written as

$$\frac{dc_1}{dx} = c_1 W_{11} + \int_0^\infty c_v(x,k)W_{1v}(x,k)\exp[\varphi_v(x,k) - \varphi_1(x)]dk +$$

$$+\int_0^\infty c_e(x,k)W_{1e}(x,k)\exp[\varphi_e(x,k) - \varphi_1(x)]dk \qquad (5.2a)$$

$$\frac{dc_v(k)}{dx} = c_1 W_{v1}\exp[\varphi_v(x,k) - \varphi_1(x)] + \int_0^\infty c_v(x,k')W_{vv}(x,k,k')\exp[\varphi_v(x,k') - \varphi_v(x,k)]dk' +$$

$$+\int_0^\infty c_e(x,k')W_{ve}(x,k,k')\exp[\varphi_e(x,k') - \varphi_v(x,k)]dk' \qquad (5.2b)$$

$$\frac{dc_e(k)}{dx} = c_1 W_{e1}\exp[\varphi_e(x,k) - \varphi_1(x)] + \int_0^\infty c_e(x,k')W_{ee}(x,k,k')\exp[\varphi_e(x,k') - \varphi_e(x,k)]dk' +$$

$$+\int_0^\infty c_v(x,k')W_{ev}(x,k,k')\exp[\varphi_v(x,k')-\varphi_e(x,k)]dk' \qquad (5.2c)$$

Accounting for the spectrum topology shown in Figures 15 and 16, we can formulate the following unit problems for the equation system (5.2):

(i) In the cross-section, $x = x_0$, located upstream from the synchronism point, $x = x_*$, disturbance spectrum contains only the first-mode wave of a unit amplitude; *i.e.*

$$c_1(x_0) = 1,\ \ c_v(x_0,k) = 0 \ \text{ and } \ c_e(x_0,k) = 0 \ \text{ for any } \ k \in [0,\infty) \qquad (5.3)$$

The first-mode wave comes into the synchronism region and excites vorticity/entropy waves propagating downstream. Find the amplitude distributions $c_v(x,k)$ and $c_e(x,k)$, as well as the first-mode wave amplitude $c_1(x)$ in the downstream region $x > x_*$.

(ii) In a cross-section, $x = x_0$, located upstream the synchronism point, $x = x_*$, disturbance spectrum contains only one vorticity wave of the wavenumber $\alpha_v = \alpha_v(k_*)$, where k_* satisfies the synchronism condition $\alpha_v(x_*,k_*) = \alpha_1(x_* + 0)$; *i.e.*

$$c_1(x_0) = 0,\ \ c_v(x_0,k) = \delta(k - k_*),\ \text{ and } \ c_e(x_0,k) = 0 \ \text{ for any } \ k \in [0,\infty) \qquad (5.4)$$

The vorticity wave comes into the synchronism region and excites the first-mode wave. Find the first-mode wave amplitude in the downstream region $x > x_*$.

(iii) In a cross-section, $x = x_0$, located upstream from the synchronism point, $x = x_*$, disturbance spectrum contains only one entropy wave of the wavenumber $\alpha_e = \alpha_e(k_*)$, where k_* satisfies the synchronism condition $\alpha_e(x_*,k_*) = \alpha_1(x_* + 0)$; *i.e.*

$$c_1(x_0) = 0, \quad c_e(x_0,k) = \delta(k-k_*), \text{ and } c_v(x_0,k) = 0 \text{ for any } k \in [0,\infty) \tag{5.5}$$

The entropy wave comes into the synchronism region and excites the first-mode wave. Find the first-mode wave amplitude in the downstream region $x > x_*$.

Rough estimates

Due to the presence of continuous spectrum it is difficult to solve Eqs. (5.2) even for relatively simple boundary conditions (5.3)-(5.5) of the unit problems (i), (ii) and (iii). We guess these problems can be simplified using asymptotic analysis of the matrix elements $W_{vv}(x,k,k')$, $W_{ve}(x,k,k')$, $W_{ee}(x,k,k')$ and $W_{ev}(x,k,k')$ as well as integrals over the continuous spectrum branches in the vicinity of synchronism point. This could be a subject for future research. However, rough estimates of coupling between the first mode and vorticity/entropy waves can be made in the following way. We introduce a virtual upper boundary, $y = y_s$, located in the inviscid flow region between the upper boundary-layer edge and the shock. On this boundary, we impose the homogeneous boundary conditions

$$z_{\alpha 1} = z_{\alpha 3} = z_{\alpha 5} = 0, \quad y = y_s \tag{5.6}$$

Now the problem (3.1a), (3.1b) and (5.6) has the non-trivial solution

$$\vec{z}_\alpha = C_1\vec{q}_1 + C_2\vec{q}_2 + C_3\vec{q}_3 + C_4\vec{q}_4 + C_5\vec{q}_5 + C_6\vec{q}_6 \tag{5.7}$$

if the determinant specified by boundary conditions is zero, *i.e.*

$$\det \begin{Vmatrix} q_{11}(0) & q_{12}(0) & q_{13}(0) & q_{14}(0) & q_{15}(0) & q_{16}(0) \\ q_{31}(0) & q_{32}(0) & q_{33}(0) & q_{34}(0) & q_{35}(0) & q_{36}(0) \\ q_{51}(0) & q_{52}(0) & q_{53}(0) & q_{54}(0) & q_{55}(0) & q_{56}(0) \\ q_{11}(y_s) & q_{12}(y_s) & q_{13}(y_s) & q_{14}(y_s) & q_{15}(y_s) & q_{16}(y_s) \\ q_{31}(y_s) & q_{32}(y_s) & q_{33}(y_s) & q_{34}(y_s) & q_{35}(y_s) & q_{36}(y_s) \\ q_{51}(y_s) & q_{52}(y_s) & q_{53}(y_s) & q_{54}(y_s) & q_{55}(y_s) & q_{56}(y_s) \end{Vmatrix} = 0 \tag{5.8}$$

The dispersion relation (5.8) leads to splitting of the continuous spectrum branches (see Fig. 1) into the discrete subsets. As the upper boundary tends to infinity, $y_s \to \infty$, these subsets thicken back into correspondent branches of continuous spectrum.

Numerical analysis of the problem (3.1a), (3.1b) and (5.6) shows that the discrete mode with the eigenvalue α_m, which belongs to the vorticity/entropy wave subset and satisfy the synchronism condition, $\alpha_m(R_*) \to \alpha_1(R_* + 0)$ as $y_s \to \infty$, transforms into the first mode in the region $R > R_*$. In a similar way, the first mode with the eigenvalue α_1 coming from the upstream region, $R < R_*$, transforms into the mode with eigenvalue α_n, which belongs to the vorticity/entropy wave subset and satisfies the synchronism condition $\alpha_n(R_*) \to \alpha_1(R_* - 0)$ as $y_s \to \infty$. These transformations are shown in Figures 18a and 18b for the upper boundary locus $y_s^* = 4\delta^*$, where δ^* is boundary layer displacement thickness. The region between the upper boundary layer edge $y = y_e$, and the virtual boundary $y = y_s$, contains about 12 wavelengths of the vorticity/entropy oscillations in the y-direction, *i.e.*

$$y_s - y_e \approx 12\frac{2\pi}{k_*} \tag{5.9}$$

where the parameter k_* correspond to the synchronism condition. Consequently, this case is a good approximation of the limit $y_s \to \infty$. In the upstream region $R < R_* \approx 1515$, the imaginary part of the normal mode eigenvalue α_m (solid line in Fig. 18b) is very close to the imaginary part of the vorticity/entropy wave eigenvalues (dashed line), which satisfy the synchronism conditions

$$\alpha_v(R_*, k_{v*}) = \alpha_1(R_* + 0), \quad \alpha_e(R_*, k_{e*}) = \alpha_1(R_* + 0) \tag{5.10}$$

These findings lead to the following conclusions:

- In the rough (of the order of magnitude) approximation, the first mode coming from the upstream region, $R < R_*$, transforms into vorticity and entropy waves with the wavenumber satisfying the synchronism condition

$$\alpha_v(R_*, k_{v*}) = \alpha_1(R_* - 0), \quad \alpha_e(R_*, k_{e*}) = \alpha_1(R_* - 0) \tag{5.11}$$

  These vorticity/entropy waves propagate downstream and slowly dissipate due to viscosity. Since this mechanism is not directly coupled with excitation of unstable normal modes, it plays a minor role in transition process.

- In the rough approximation, the vorticity/entropy waves coming from the upstream region, $R < R_*$, and satisfying the synchronism condition (5.10), transform into the first mode propagating downstream, $R > R_*$. If the vorticity/entropy eigenfunctions $\vec{A}_v(x,y)$ and $\vec{A}_e(x,y)$ are normalized similar to the first mode eigenfunction $\vec{A}_1(x,y)$, say the disturbance pressure amplitude on the wall $A_{v4}(x,0) = A_{e4}(x,0) = A_{14}(x,0) = 1$, then the vorticity wave of the amplitude $c_v(R_* - 0)$ generates the first mode wave of the amplitude

$$|c_1(R_* + 0)| \approx |c_v(R_* - 0)| \tag{5.12}$$

  In a similar way, the entropy wave of the amplitude $c_e(R_* - 0)$ generates the first mode wave of the amplitude

$$|c_1(R_* + 0)| \approx |c_e(R_* - 0)| \tag{5.13}$$

Further downstream (see Region 3 in Figures 2 and 5) the first mode is synchronized with the second mode. As it was shown in Section 4, the first mode wave excites the second mode wave of the amplitude

$$|c_2(R_{b1}+0)|\approx|c_1(R_{b1}-0)| \tag{5.14}$$

where R_{b1} is the branch point located in Region 3. Since the first mode attenuation is relatively weak in a distance between points R_* and R_{b1}, we can estimate the first-mode wave amplitude as

$$|c_1(R_{b1}-0)|\approx|c_1(R_*+0)| \tag{5.15}$$

Finally, using Eqs. (5.6), (5.7), (5.11) and (5.12) we estimate the initial amplitude of the normal mode waves as

$$|c_1(R_{b1}+0)|\approx|c_2(R_{b1}+0)\approx|c_v(R_*-0)| \text{ or } |c_2(R_{b1}+0)|\approx|c_2(R_{b1}+0)\approx|c_e(R_*-0)| \tag{5.16}$$

where c_v and c_e are amplitudes of the vorticity and entropy wave satisfying the synchronism condition (5.4) in Region 2. As shown in Section 4, one of these normal waves gets essentially unstable downstream from the branch point R_{b1}. This is the Mack's second-mode instability. Its initial amplitude at the branch point R_{b1} can be roughly estimated using the relations (5.16). These estimates show that the vorticity (entropy) waves of a frequency ω and the wavenumber α_v (α_e), which satisfy the synchronism condition (5.5), are "swallowed" by the boundary layer in the synchronism Region 2 and generates the unstable normal waves of the same frequency. Sketch of this swallowing mechanism is shown in Fig. 19. The unstable-wave initial amplitude of some physical value, $Q_{unstable}$, measured at the branch point $R=\mathrm{Re}(R_{b1}(\omega))$, is approximately equal to the amplitude of said vorticity

(entropy) wave, Q_v (Q_e), measured near the synchronism point $R_*(\omega) - 0$. In wind tunnel experiments, vorticity (entropy) wave amplitude near the synchronism point R_*, Q_v (Q_e), can be measured using a hot-wire anemometry with streamwise and vertical probe separation [42] or hot films placed on the wall near the synchronism point R_*. Coupling between vorticity/entropy waves and the Mack's second mode can be verified by correlation measurements.

It is generally believed that for the case of hypersonic wind tunnels, the major source of freestream disturbances is from the radiation of sound generated by the turbulent boundary layer on the wind tunnel nozzle walls. However, most of the acoustic energy is concentrated at low frequencies, and sound amplitudes decreases with increasing frequency. For thin boundary layers at high unit Reynolds numbers, the second-mode waves may have frequencies, which are larger than the frequencies where the freestream sound is lost in the electronic noise. Therefore, a conventional hypersonic wind tunnel may be "quiet" for the second mode disturbances [26]. In this case, the freestream entropy and vorticity disturbances may play a major role in the boundary-layer transition. Similar situation may occur in flight conditions due to the presence of atmospheric turbulence and the absence of freestream acoustic disturbances. The transition onset point can be correlated with the freestream vorticity and entropy disturbances using the PSE method [19] with the initial amplitude distribution of the Mack's second mode being estimated as

$$Q_{unstable}(R_{b1}(\omega)) = Q_v(R_*(\omega) - 0) \text{ and/or } Q_{unstable}(R_{b1}(\omega)) = Q_e(R_*(\omega) - 0) \qquad (5.17)$$

Here Q_v and Q_e are amplitudes of the vorticity and entropy wave satisfying the synchronism condition (5.10) in Region 2.

Foregoing analysis addresses the entropy/vorticity waves, which are strictly satisfy the synchronism conditions, and does not account for neighboring waves. Additional exchange between normal modes and the vorticity/entropy waves, which are slightly de-tuned from the

synchronism , may affect the initial amplitude of unstable normal waves. However, rough estimates (5.17) can be useful for the transition onset prediction due to the following reasons. According to the amplitude method [21], the transition onset point x_{tr} is determined from the equation

$$-\int_{x_{in}}^{x_{tr}} \alpha_i dx = \ln\left(\frac{A_{cr}}{A_{in}}\right) \tag{5.18}$$

where $-\alpha_i$ is spatial growth rate, x_{in} is locus of the instability growth onset, A_{in} is initial amplitude, and A_{cr} is critical amplitude related to the beginning of nonlinear processes. Since the transition point depends weakly (as a logarithm) on the initial amplitude value, even rough estimates of A_{in} can provide sufficient accuracy for the transition onset prediction. Such estimates can be economically made using the coupling (5.17) and integrated into stability codes.

6. Summary discussion and future effort

Transition process is an initial boundary value problem, which requires distributions of the normal mode amplitudes at the instability growth onset. These initial data are determined from receptivity analysis comprising the identification of external disturbances, the determination of the most sensitive regions, and prediction of the normal mode propagation from these regions to the instability growth onset (instability pre-history). Foregoing analysis shows that all these elements are different from those typical for subsonic and moderate supersonic speeds. Low supersonic stability concepts cannot be just extended to hypersonic cases. The multiple-mode method rather than a single-mode approach is required to evaluate receptivity and instability pre-history of hypersonic boundary layers. These phases of the transition process are more complicated than in moderate supersonic cases due to the

presence of the disturbance spectrum singularities. As shown in Figures 3a and 6a, these singularities are located in:

- the nose region 1, where the first and second waves are synchronized with external acoustic waves of the phase speed $c_r = 1 + 1/M_e$ and $c_r = 1 - 1/M_e$ respectively.
- the synchronism region 2, where the first mode is synchronized with the external entropy/vorticity waves of the phase velocity $c_r = 1$. In this region, the first mode penetrates outside the boundary layer. Its oscillating "tail" (see Fig. 5) could be identified by measuring correlations between hot-wire signals inside and outside the boundary layer.
- the synchronism region 3, where the first and second modes are synchronized near the branch point of discrete spectrum. In this region, the boundary-layer disturbance field has abnormal behavior, which could be detected using the hot-wire measurements.

In the nose region 1, acoustic waves can effectively excite the first and second modes [32], [35]. This receptivity mechanism is qualitatively different from the subsonic case reviewed by Choudhari [18]. In conventional hypersonic wind tunnels, freestream acoustic waves are generated by sources propagating in the turbulent boundary layer on nozzle walls. These waves have the phase speed $c < 1 - 1/M_e$, and do not satisfy the synchronism condition. However, their interaction with the nose tip induces a local source, which generates "dangerous" disturbances of the phase speed $c = 1 \pm 1/M_e$, as schematically shown in Fig. 4. For a planar configuration (flat plate or hollow cylinder), this acoustic source is concentrated at the leading edge. For the conical flow, it is concentrated near the cone tip. Since the point source is weaker than the line source and downstream attenuation of acoustic energy from the point source is stronger than that from the line source, receptivity of a planar configuration to acoustic disturbances should be higher than that of a conical configuration. These arguments are consistent with experimental observations [33]. The freestream acoustic scattered by sharp leasing edges can be used to create a source

providing disturbances of the frequency and amplitude under control. Schemes of such a disturbance generator are shown in Figures 20a and 20b. When an external acoustic source (A) is placed below the model axis (see Fig. 20a), then it induces an acoustic source of the same frequency at the leading edge. Acoustic disturbances from the leading edge source penetrate into the boundary layer, whereas the other portion of disturbances is blocked by the body and do not affect the boundary layer. As contrasted to natural transition experiments, this scheme allows direct measurements of the hypersonic leading edge receptivity and downstream evolution of the boundary-layer disturbances. If the external acoustic source (B) is placed above the model as shown in Fig. 20b, then the boundary layer is radiated by acoustic waves from both Source (B) and the leading edge source. Comparing these two cases we could estimate the leading edge receptivity versus the distributed receptivity.

In the synchronism region 2, vorticity and entropy waves are partially swallowed by the boundary layer and effectively generate the first mode as schematically shown in Fig. 19. This receptivity mechanism can compete with the leading edge receptivity to freestream acoustic disturbances in cases when:

- acoustic disturbances are small compared to freestream turbulence and temperature spottiness in the frequency band of the boundary-layer instability. Low level of freestream noise is typical for flight conditions. Moreover, Stetson and Kimmel [26] noted that for the wind tunnel experiments at high Reynolds numbers, the boundary-layer instability may have frequencies, which are larger than frequencies where the freestream noise is lost in the electronic noise. Therefore, even conventional hypersonic wind tunnels may be "quiet" in the instability frequency band.
- the leading edge shape corresponds to relatively weak interaction between external acoustic field and the boundary layer. The sharp cone is a good example of this case. In contrast to the conical flow, a planar configuration (flat plate or hollow cylinder) can create a strong local source at the leading edge due to external acoustic scattering. Since

the point source on the cone tip is weaker than the line source on a plate leading edge and downstream attenuation of the acoustic energy from the point source is stronger than that from the line source, receptivity of a planar configuration to acoustic disturbances should be higher than that of a conical configuration. These arguments are consistent with experimental observations [33].

Analysis of Section 5 provides rough estimates for coupling between the external vorticity/entropy disturbances and the initial amplitude of hypersonic boundary-layer instability. These results can be used as initial data for the PSE analysis downstream from the synchronism region 2. Since the transition point depends weakly (as a logarithm) on the initial amplitude of the boundary-layer instability, even rough estimates of the receptivity mechanism can provide sufficient accuracy for the transition onset prediction. Such estimates can be economically made using the coupling relation (5.17) and integrated into stability codes such as the PSE code. That makes feasible an amplitude method for the transition prediction coupling receptivity and stability problems.

In the synchronism region 3, characteristics of the first mode are very close to those of the second mode. The discrete spectrum has the branch point R_{b1} located in the complex R-plane near the real axis. Near the branch point the discrete spectrum splits into two branches, as schematically shown in Fig. 7. Instability of the Mack's second mode is associated with this splitting. In the vicinity of the branch point, the normal mode decomposition is not valid and should be replaced by local solution, which provides coupling between input and output amplitudes. In the first order approximation, the inter-mode exchange rule (4.21) does not depend on the mean flow profiles and can be applied for broad class of shear layers with similar topology of the discrete spectrum.

Calculations of the branch point R_{b1} as a function of the disturbance frequency, local Mach number and wall temperature ratio show that the branch point can intersect the real axis (see

Fig. 13b). That leads to different topology of the discrete spectrum splitting. If the branch point is in the upper half of the complex R-plane, it is bypassed from lower side as the Reynolds number increases along the real axis. Downstream from the branch point, the first mode gets essentially unstable and the second mode gets more stable. This case is shown in Figures 6a and 6b and corresponds to the cooled wall cases of relatively low Mach numbers, $M_e < 6$. If the branch point is in the lower half plane, it is bypassed from the upper side. Downstream from the branch point, the second mode gets unstable and the first mode gets more stable. This case is shown in Figures 3a and 3b. Infinitesimal variation of the basic parameter (say the Mach number M_e) near the value at which the branch point crosses the real axis causes jump from one topology to another. Moreover, near the branch point the normal wave amplitude tends to infinity and the group velocity has non-monotonic behavior. These features along with the spectrum singularity in the synchronism region 2 can cause significant difficulties in the PSE integration as well as stability calculations using the e^{Malik} or COSAL codes.

Summarizing we can formulate the following possible scenario of the transition initial phase:

External entropy/vorticity disturbances generate the first mode in the synchronism region 2. This mode excites the second mode near the branch point R_{b1} of the synchronism region 3. Receptivity and the inter-mode exchange mechanisms relevant to these regions provide initial amplitude for the Mack's second mode just near the instability growth onset. Further downstream, the Mack's second mode amplifies up to the critical amplitude corresponding the transition onset.

This scenario is more probable for the conical configurations and "quiet" freestream conditions. It is consistent with the following experimental observations:

- Transition on a sharp cone is less sensitive to the cone tip conditions (wall temperature jump, small bluntness) than transition on a flat plate.

- Hypersonic cone transition data [25] do not fit to the correlation of Pate and Scheuler based on assumption that external acoustic waves trip the boundary layer (see [44]).
- Since the Mack's second-mode waves are excited just near the instability onset, they start to grow with the initial amplitude to be relatively slow function of the disturbance frequency. These waves become "tuned" to the boundary layer thickness and tend to the optimal tuning near the envelope curve. That is consistent with experimental data reported in [26].

This study is only the first step in understanding of hypersonic boundary-layer receptivity and instability pre-history. However, it provides good starting conditions to attack the following challenging problems:

- Foregoing analysis should be extended to the three-dimensional disturbance case. Wave packets rather than plane waves need to be addressed. That will help to evaluate receptivity to 3-D freestream disturbances and downstream propagation of unstable wave packets typical for a hypersonic wind tunnel transition.
- Receptivity to vorticity/entropy waves needs to be studied in detail. Rough estimates of receptivity mechanism should be refined from systematic analysis of the unit problems formulated in Section 5.
- The flat-plate leading edge receptivity model [32], [35] should be extended to the conical configurations and the blunt leading edge cases.

Investigation of these problems will help to explain hypersonic stability and transition experiments and develop reliable transition prediction methods required for hypersonic vehicle design.

Acknowledgments

The support by Dr. Roger Kimmel who kindly provided experimental data and discussed the results is gratefully acknowledged. We also thank Dr. Jonathan Poggie for useful discussions. The work was sponsored by the European Office of Aerospace Research and Development of the Department of the Air Force under Contract F61708-96-W0196. We appreciate the support provided by Drs. Mark Maurice and Charbel Raffoul.

References

1. Finley, D. "Hypersonic Aerodynamic Considerations and Challenges," AIAA Paper, No. 90-5222, Oct. 1990.
2. Goodrich, Winston D., Derry, Stephen M., and Maraia, Robert J. "Effects of Aerodynamic Heating and TPS Thermal Performance Uncertainties on the Shuttle Orbiter," *Progress in Astronautics and Aeronautics*, Vol. 69, Martin Summerfield, Series Editor-in-Chief, New York, NY, 1979.
3. Malik, M., Zang, T., and Bushnell, D, "Boundary Layer Transition in Hypersonic Flows," AIAA Paper No. 90-5232, 1990.
4. Morkovin, M.V., "Critical Evaluation of Transition from Laminar to Turbulent Shear Layers with Emphasis on Hypersonically Traveling Bodies," AFFDL-TTR 68-149, Air Force Flight Dynamics Laboratory, Wright Patterson Air Force Base, Dayton, Ohio, 1969.
5. Reshotko, E., "Boundary Layer Stability and Transition," *Ann. Rev. Fluid Mech.*, vol. 8, pp. 311-349, 1976.
6. Mack, L.M., "Boundary Layer Linear Stability Theory," AGARD Report No. 709, June 1984.
7. Malik, M.B., "Prediction and Control of Transition in Supersonic and Hypersonic Boundary Layers," *AIAA Journal*, vol. 27, No. 11, pp. 1487-1493, 1989.
8. Reshotko, E., "Boundary Layer Instability, Transition and Control," AIAA Paper No. 94-0001, 1994.
9. Kachanov, Yu.S., Kozlov, V.V., and Levchenko, V.Ya., *Occurrence of Turbulence in Boundary Layer*, Nauka, Novosibirsk, 1982 (in Russian).
10. Gaponov, S.A., Maslov, A.A., *Development of Disturbances in Compressible Flows*, Nauka, Novosibirsk, 1980 (in Russian).
11. Kosinov, A.D., Maslov, A.A., and Shevel'kov S.G., "Experiments on the Stability of Supersonic Laminar Boundary Layers," *J. of Fluid Mech.*, vol. 219, pp. 621-633, 1990.

12. Zhigulev, V.N., and Tumin, A.M., *Origin of Turbulence*, Nauka, Novosibirsk, 1987 (in Russian).
13. Goldstein, M.E., "The Evolution of Tollmien-Schlichting Waves near a Leading Edge," *J. of Fluid Mech.*, vol. 127, pp. 59-81, 1983.
14. Kendall, J.M., "Boundary Layer Receptivity to Freestream Turbulence," AIAA Paper No. 90-1504, 1990.
15. Choudhari, M., and Streett, C., "Boundary Layer Receptivity Phenomena in Three-Dimensional and High-Speed Boundary Layers," AIAA Paper No. 90-5258, 1990.
16. Saric, W.S., and Reed, H.L., "Leading Edge Receptivity to Sound: Experiments, DNS, and Theory," AIAA Paper No. 94-2222, 1994.
17. Choudhari, M., "Boundary-Layer Receptivity to Three-Dimensional Unsteady Vortical Disturbances in Free Stream," AIAA Paper No. 96-0181, 1996.
18. Choudhari, M., "Theoretical Prediction of Boundary-Layer Receptivity," AIAA Paper No. 94-2223, 1994.
19. Bertolotti, F.P., and Herbert, Th., "Analysis of the Linear Stability of Compressible Boundary Layers Using the PSE," *Theoretical and Computational Fluid Dynamics*, vol. 3, pp. 117-124, 1991.
20. Chang, C.-L., Malik, M.R., "Compressible Stability of Growing Boundary Layers Using Parabolized Stability Equations," AIAA Paper No. 91-1636, 1991.
21. Mack, L.M., "A Numerical Method for the Prediction of High Speed Boundary-Layer Transition Using Linear Theory, " In: NASA SP-347, pp. 101-123, 1975.
22. Mack, L.M., "Boundary-Layer Stability Theory," Part B, Doc. 900-277, JPL, Passadena, California, May 1969.
23. Kendall, J. M., "Wind Tunnel Experiments Relating to Supersonic and Hypersonic Boundary Layer Transition," *AIAA Journal*, vol. 13, No. 3, pp. 290-299, 1975.
24. Demetriades, A., "Hypersonic Viscous Flow over a Slender Cone, Part III: Laminar Instability and Transition," AIAA Paper No. 74-535, 1974.

25. Stetson, K. F., Thompson, E. R., Donaldson, J. C., and Siler, L. G., "Laminar Boundary Layer Stability Experiments on a Cone at Mach 8. Part 1: Sharp Cone," AIAA Paper No. 83-1761, 1983.

26. Stetson, K.F., and Kimmel, R.L., "The Hypersonic Boundary-Layer Stability," AIAA Paper, No. 92-0737, January, 1992.

27. Mack, L. M., "Stability of Axisymmetric Boundary Layers on Sharp Cones at Hypersonic Mach Numbers," AIAA Paper No. 87-1413, 1987.

28. Simen, M., and Dallmann, U., "On the Instability of Hypersonic Flow Past a Pointed Cone - Comparison of Theoretical and Experimental Results at Mach 8," AGARD Symposium on Theoretical and Experimental Methods in Hypersonic Flows, Torino, Italy, 4-7 May 1992.

29. Gasperas, G., "Effect of Wall Temperature Distribution on the Stability of Compressible Boundary Layer," AIAA Paper No. 89-1894, 1989.

30. Gischin, V.R., and Fedorov, A.V., "Qualitative Properties of the Instability of Currents at a Wall in the Presence of a Flow at High Supersonic Speeds," *Modeli Mekhaniki Neodnorod. Sisitem*, ITPM SO AN SSSR, Novosibirsk, pp. 93-116, 1989 (in Russian). See also translation in NASA TT 20683, April 1990.

31. Guschin, V.R., Fedorov, A.V., "Excitation and Development of Unstable Disturbances in Supersonic Boundary Layer," *Izv. Akad. Nauk SSSR, Mekh. Zhidk. i Gaza*, No. 3, pp. 21-29, 1990.

32. Fedorov, A.V., and Khokhlov, A.P., "Excitation and Evolution of Unstable Disturbances in Supersonic Boundary Layer," *Proc. of 1993 ASME Fluid Engineering Conference*, Washington, DC, June 20-24, 1993, FED-Vol. 151, Transitional and Turbulent Compressible Flows, ASME 1993, pp.1-13, 1993.

33. Stetson, K. F., Kimmel, R. L., Thompson, E. R., Donaldson, J. C., and Siler, L. G., "A Comparison of Planar and Conical Boundary Layer Stability and Transition at a Mach Number of 8," AIAA Paper No. 91-1639, 1991.

34. Mack, L. M., "Linear Stability Theory and the Problem of Supersonic Boundary-Layer Transition," *AIAA Journal*, Vol. 13, No. 3, pp. 278-289, 1975.

35. Fedorov, A.V., and Khokhlov, A.P., "Excitation of Unstable Modes in a Supersonic Boundary Layer by Acoustic Waves," *Izv. AN SSSR, Mekhanika Zhidkosti i Gaza*, No. 4, pp. 67-74, 1991.

36. Kosinov, A.D., Institute of Theoretical and Applied Mechanics of SRAN (privet communication).

37. Zhigulev, V.N., Sidorenko, N.V., and Tumin, A.M., "Generation of Instability Waves in a Boundary Layer by External Turbulence," *J. Appl. Mech. Tech. Phys.*, **21**, 774, 1980.

38. Fedorov, A.V., "Excitation and Development of Unstable Waves in a Compressible Boundary Layer," Ph. D. Diss., Moscow Institute of Physics and Technology, 1982 (in Russian).

39. Tumin, A.M., and Fedorov, A.V., "Spatial Growth of Disturbances in a Compressible Boundary Layer," *J. Appl. Mech. Tech. Phys.*, vol. 24, p. 548, 1983.

40. Tumin, A.M., "Excitation of Tollmien-Schlichting Waves in the Boundary Layer by the Vibrating Surface of an Infinite Span Delta Wing," *J. Appl. Mech. Tech. Phys.*, vol. 23, pp. 670-674, 1982.

41. Nayfeh, A.H., "Stability of Three-Dimensional Boundary Layer," AIAA Journal, vol. 18, No. 4, pp. 406-416, 1980.

42. Hayes, W.D., and Probstein, R.F., *Hypersonic Flow Theory*, Academic Press, New York and London, 1959.

43. Fedoruk, M.V., *Asymptotic Methods for Ordinary Differential Equations*, Nauka, Moscow, 1983 (in Russian).

44. Kimmel, R., Demetriades, A., and Donaldson, J., "Space-Time Correlation Measurements in a Hypersonic Transitional Boundary Layer," AIAA Paper, No. 95-2292, 1995.

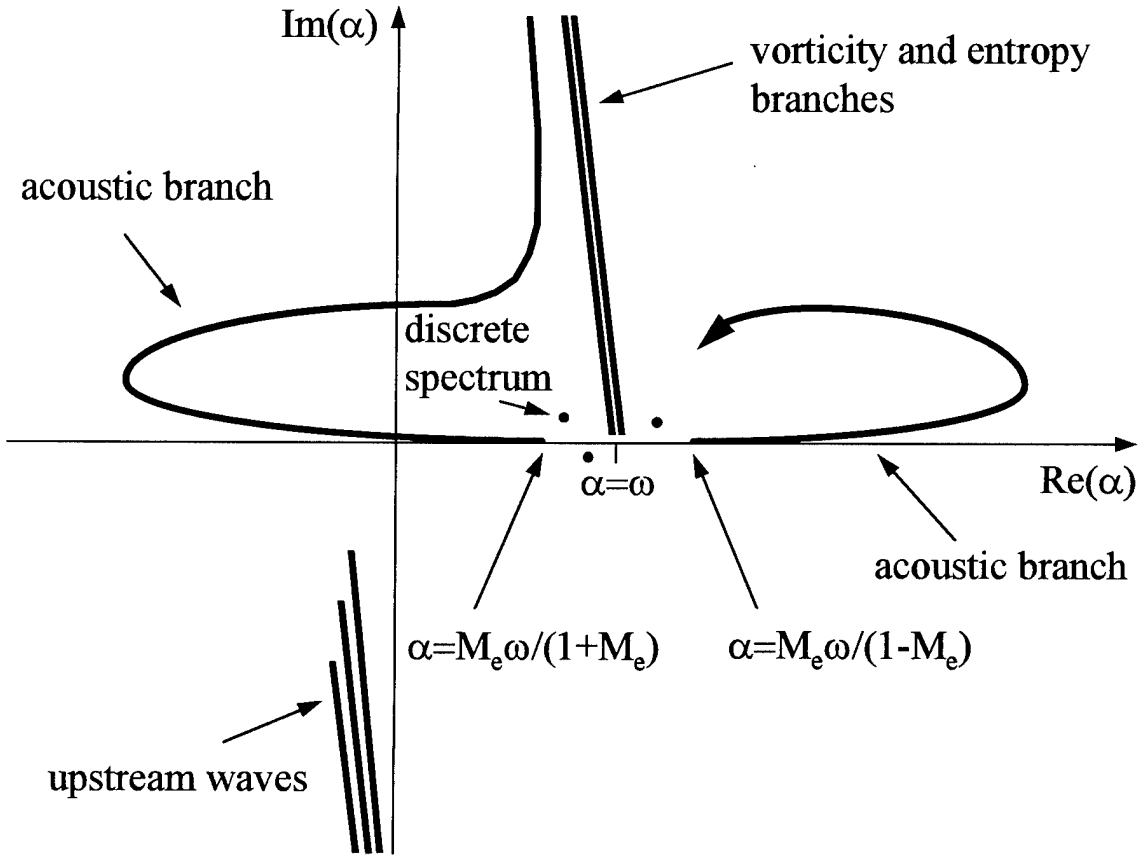

Fig. 1 Disturbance spectrum topology for supersonic boundary layer.

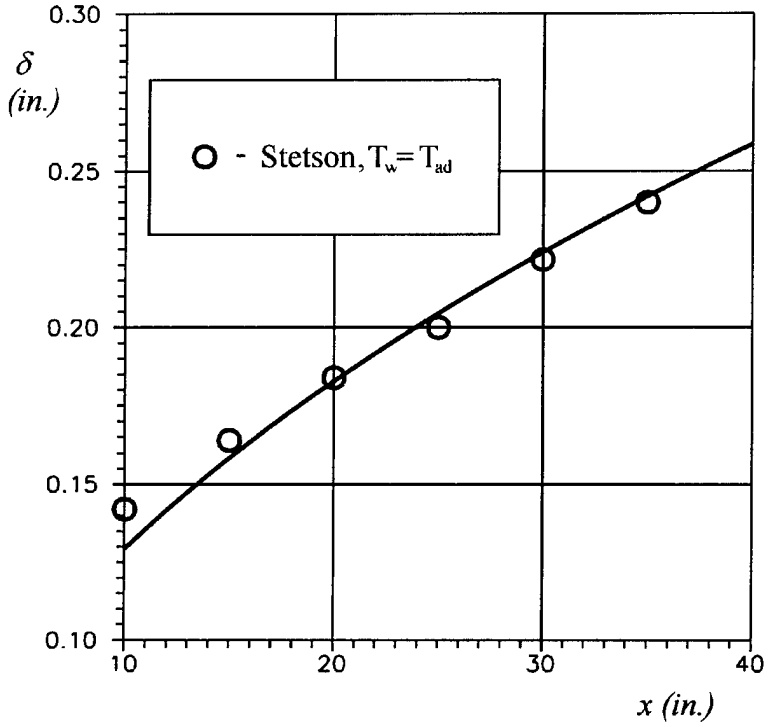

Fig. 2 Boundary-layer thickness distribution on a sharp 7-degree half angle cone at zero angle of attack; $M_e = 6.8$, $T_w = T_{ad}$.

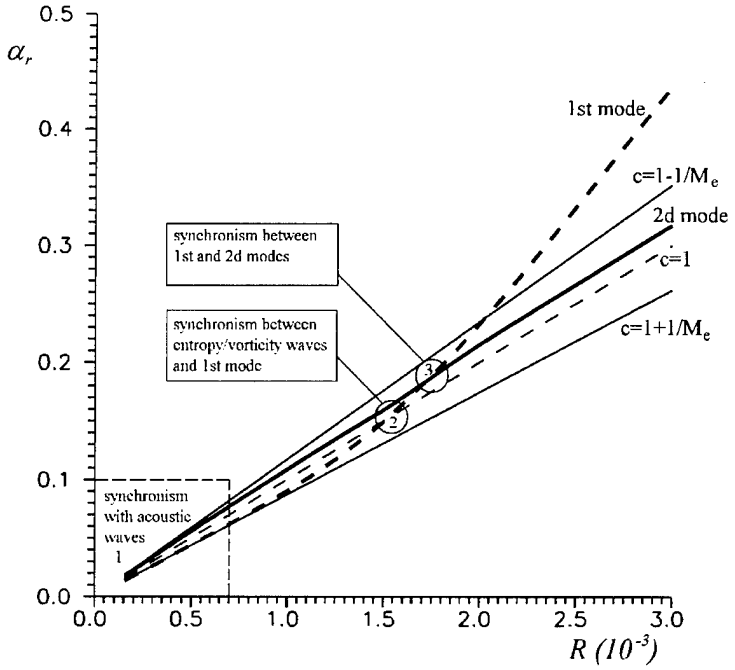

Fig. 3a Disturbance spectrum for the conical boundary layer at $F = 10^{-4}$; $M_e = 6.8$, $T_w = T_{ad}$; the eigenvalue real part distributions $\alpha_r(R)$.

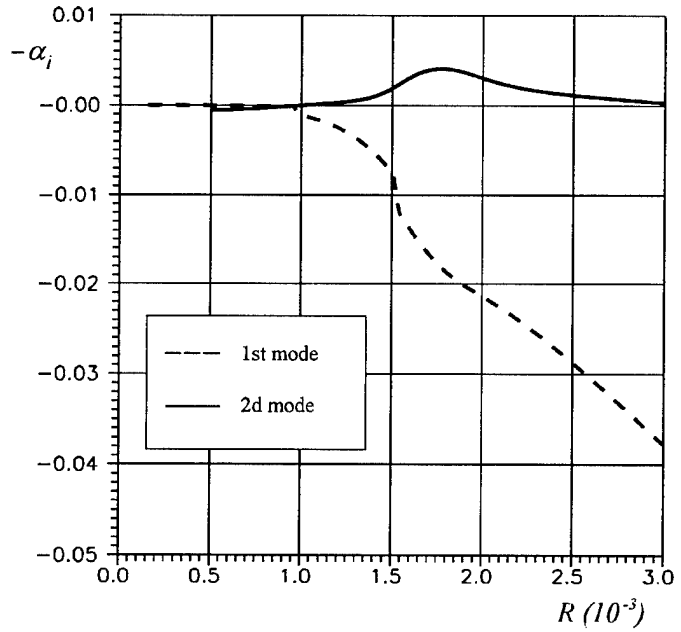

Fig. 3b Disturbance spectrum for the conical boundary layer at $F = 10^{-4}$; $M_e = 6.8$, $T_w = T_{ad}$; the eigenvalue imaginary part distributions $\alpha_i(R)$.

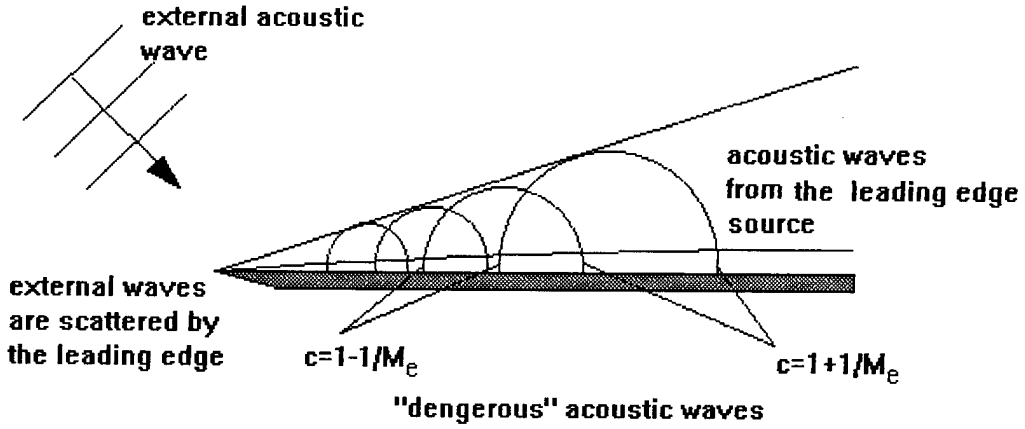

Fig. 4 Schematic pattern of interaction between an external acoustic wave and the leading edge.

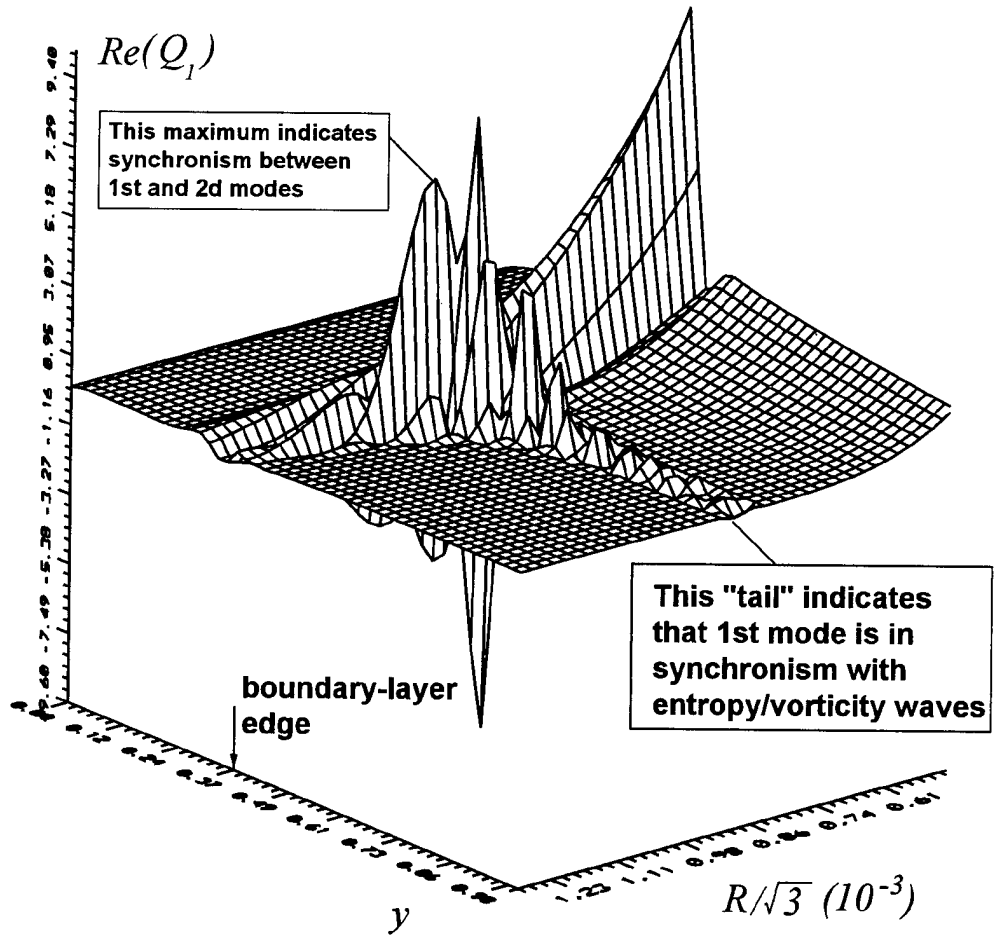

Fig. 5 The first mode eigenfunction for the conical boundary layer at $F = 10^{-4}$; $M_e = 6.8$, $T_w = T_{ad}$.

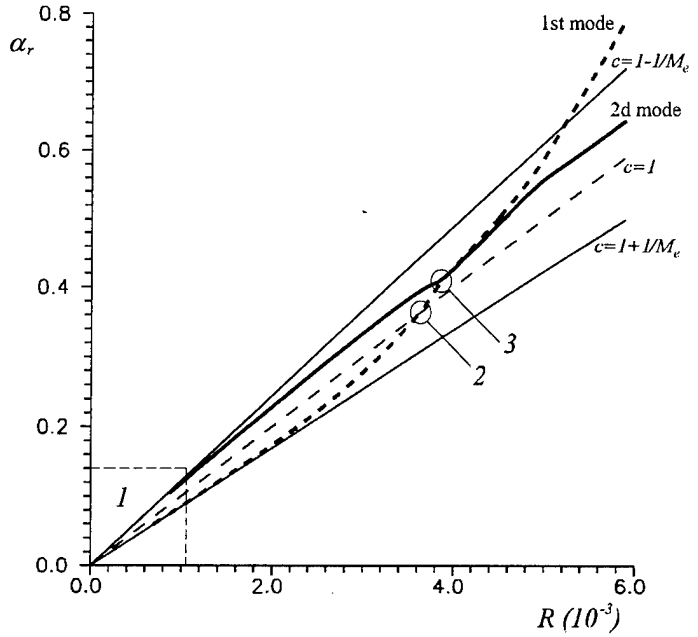

Fig. 6a Disturbance spectrum for the conical boundary layer at $F = 10^{-4}$; $M_e = 5.5$, $T_w / T_{ad} = 0.1$; the eigenvalue real part distributions $\alpha_r(R)$.

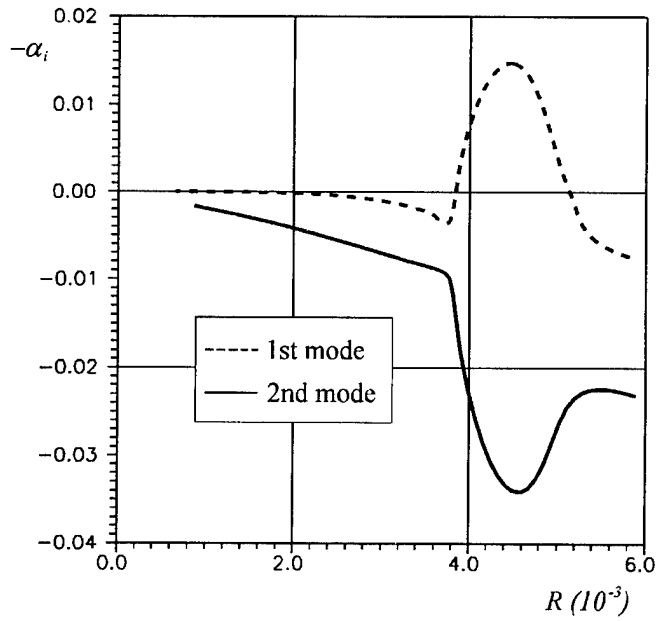

Fig. 6b Disturbance spectrum for the conical boundary layer at $F = 10^{-4}$; $M_e = 5.5$, $T_w / T_{ad} = 0.1$; the eigenvalue imaginary part distributions $\alpha_i(R)$.

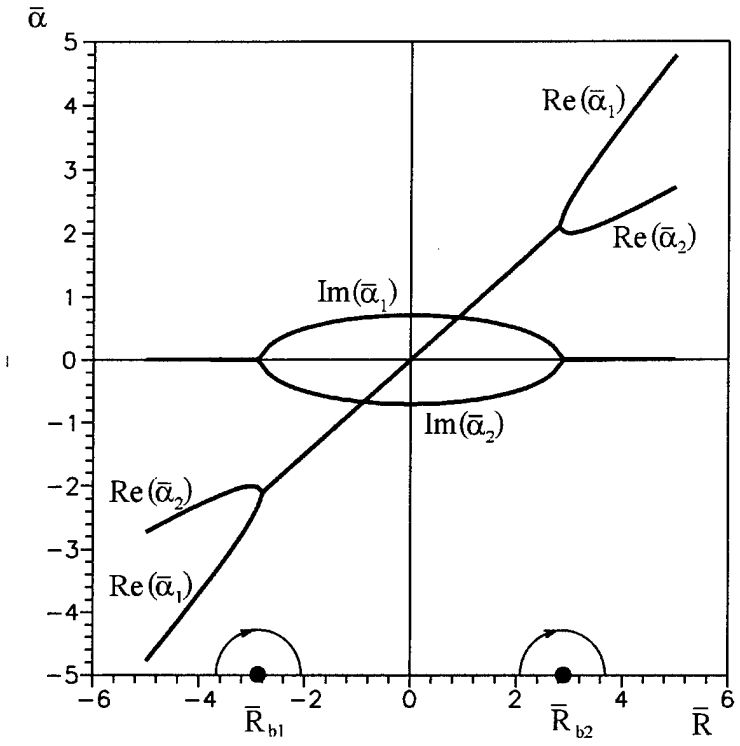

Fig. 7 Topology of the dispersion relation (4.1) in the synchronism region.

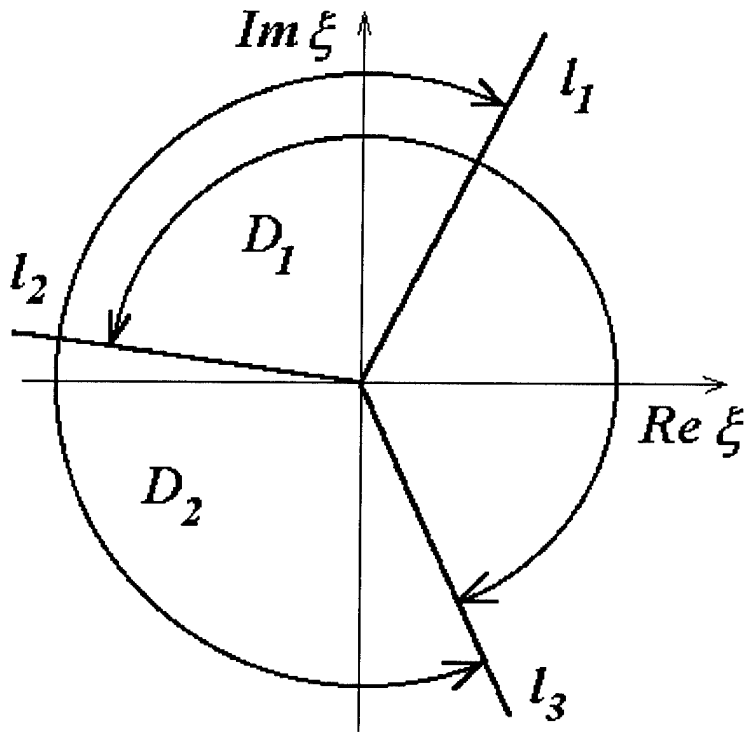

Fig. 8 Stokes lines l_j and canonical domains D_j in the branch point vicinity.

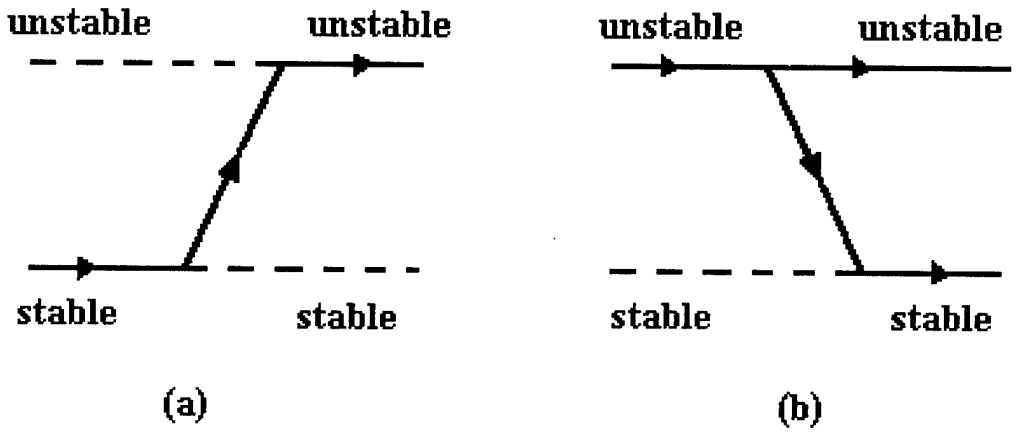

Fig. 9 The inter-mode exchange diagrams; (a) - stable mode transformation; (b) - unstable mode transformation.

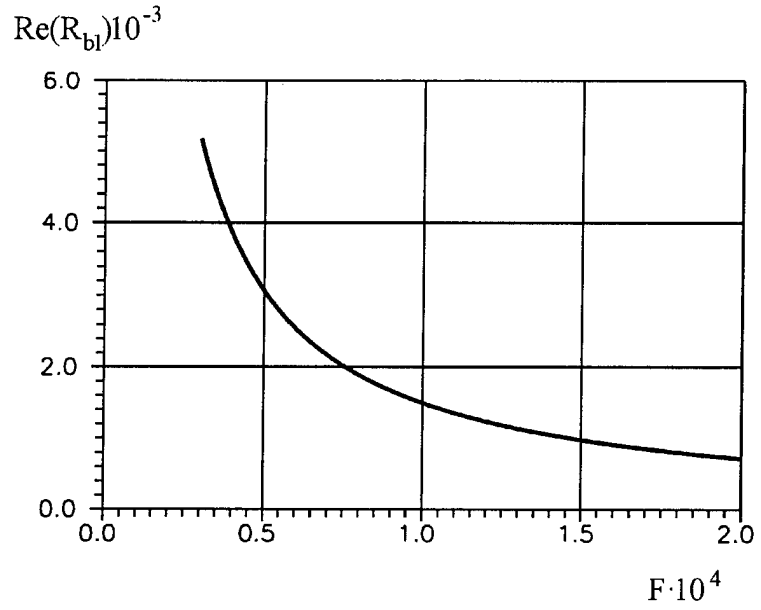

Fig. 10a Real part of the branch point R_{b1} as a function of the frequency parameter F; $M_e = 6.8$, $T_w = T_{ad}$.

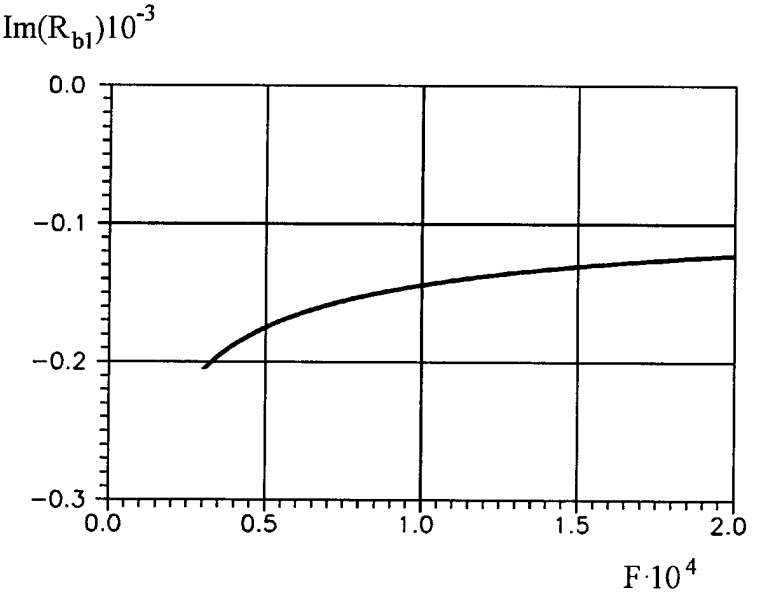

Fig. 10b Imaginary part of the branch point R_{b1} as a function of the frequency parameter F; $M_e = 6.8$, $T_w = T_{ad}$.

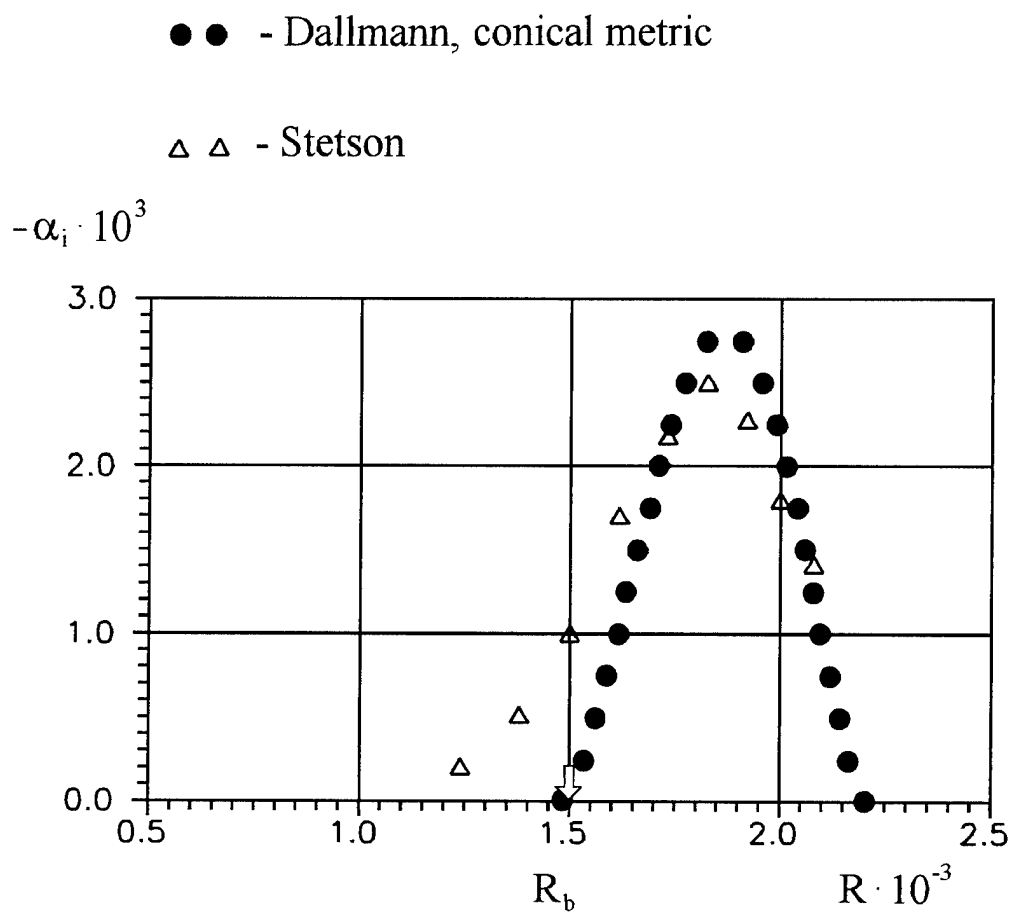

Fig. 11 Location of the branch point R_{b1} compared to experimental data of Stetson *et al.* [25] and linear stability calculations of Simen and Dallmann [28]; $M_e = 6.8$, $T_w = T_{ad}$, $F = 10^{-4}$.

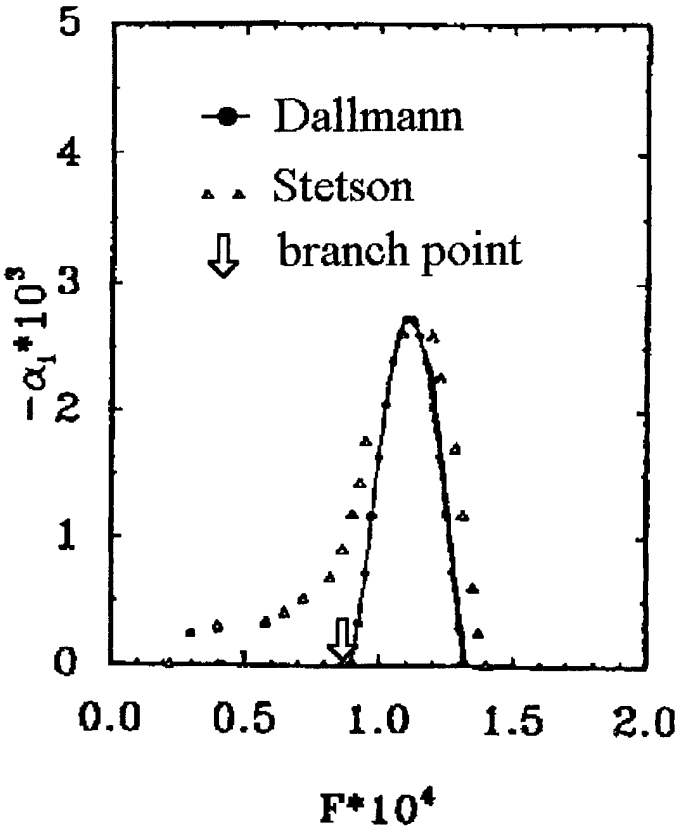

Fig. 12 Location of the branch frequency compared to experimental data of Stetson *et al.* [25] and linear stability calculations of Simen and Dallmann [28]; $M_e = 6.8$, $T_w = T_{ad}$, $R = 1731$.

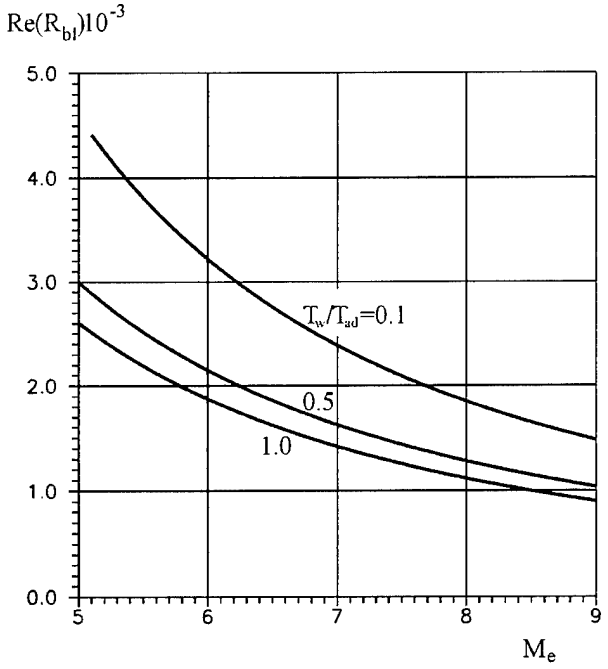

Fig. 13a Real part of the branch point R_{b1} as a function of the local Mach number M_e at various wall temperature ratios T_w / T_{ad}; $F = 10^{-4}$.

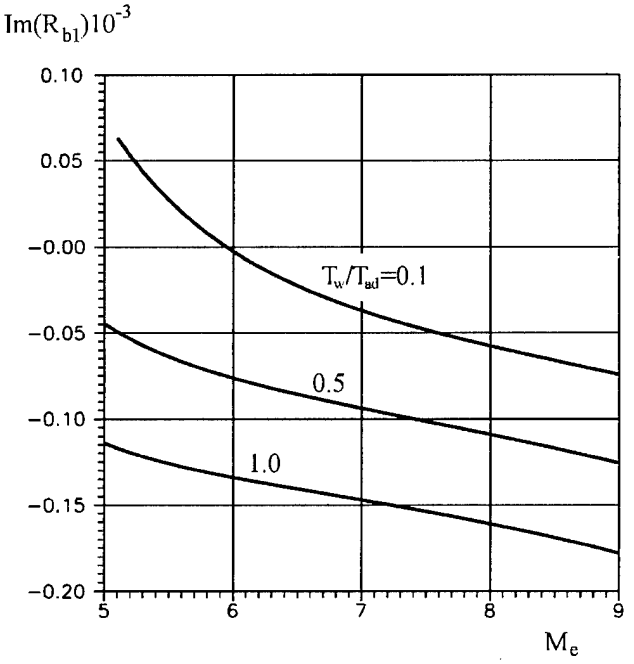

Fig. 13b Imaginary part of the branch point R_{b1} as a function of the local Mach number M_e at various wall temperature ratios T_w / T_{ad}; $F = 10^{-4}$.

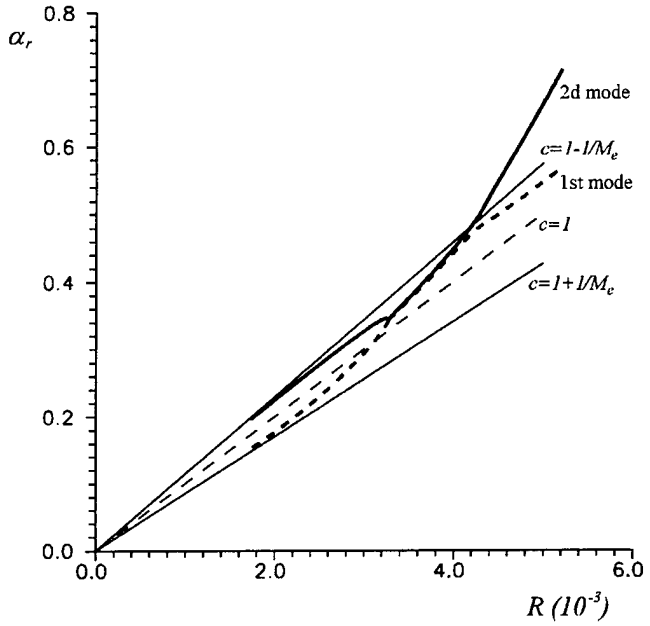

Fig. 14a Disturbance spectrum for the conical boundary layer at $F = 10^{-4}$; $M_e = 5.95$, $T_w / T_{ad} = 0.1$; the eigenvalue real part distributions $\alpha_r(R)$.

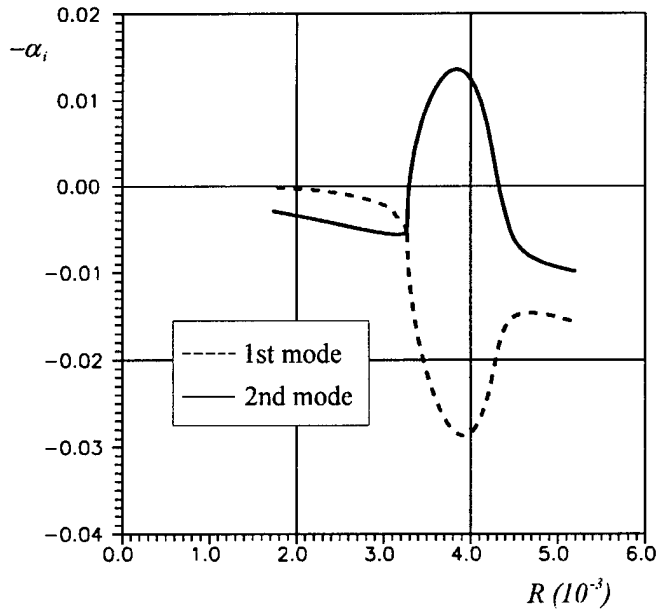

Fig. 14b Disturbance spectrum for the conical boundary layer at $F = 10^{-4}$; $M_e = 5.95$, $T_w / T_{ad} = 0.1$; the eigenvalue imaginary part distributions $\alpha_i(R)$.

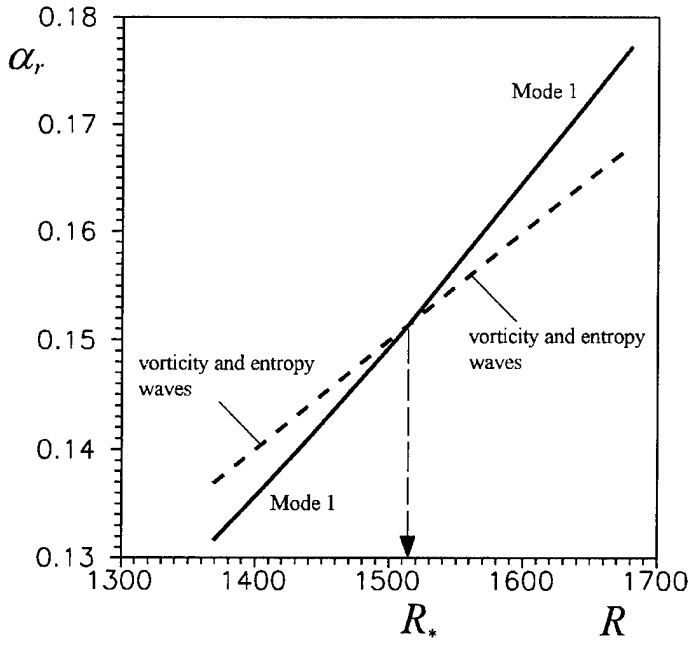

Fig. 15a Disturbance spectrum $\alpha_r(R)$ in the vicinity of synchronism point $R_* \approx 1515$; $M_e = 6.8$, $T_w = T_{ad}$.

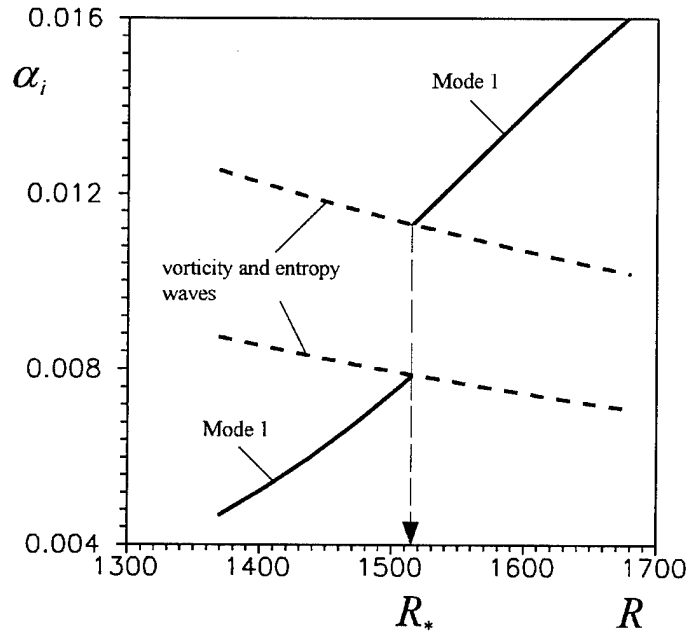

Fig. 15b Disturbance spectrum $\alpha_i(R)$ in the vicinity of synchronism point $R_* \approx 1515$; $M_e = 6.8$, $T_w = T_{ad}$.

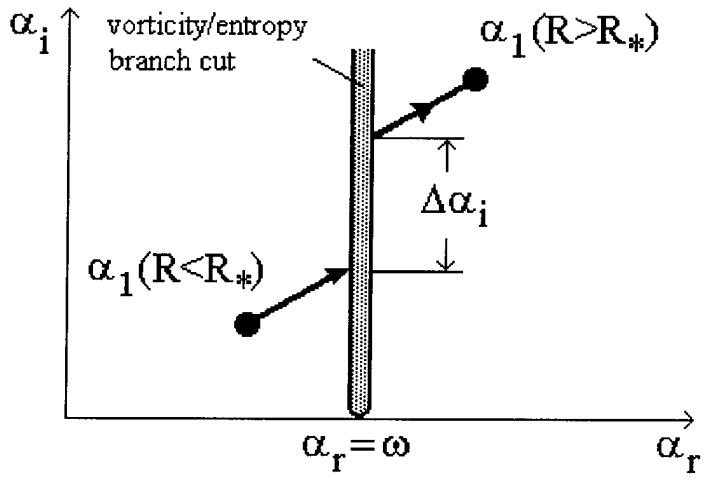

Fig. 16 Spectrum topology in the complex α-plane near the synchronism point R_*.

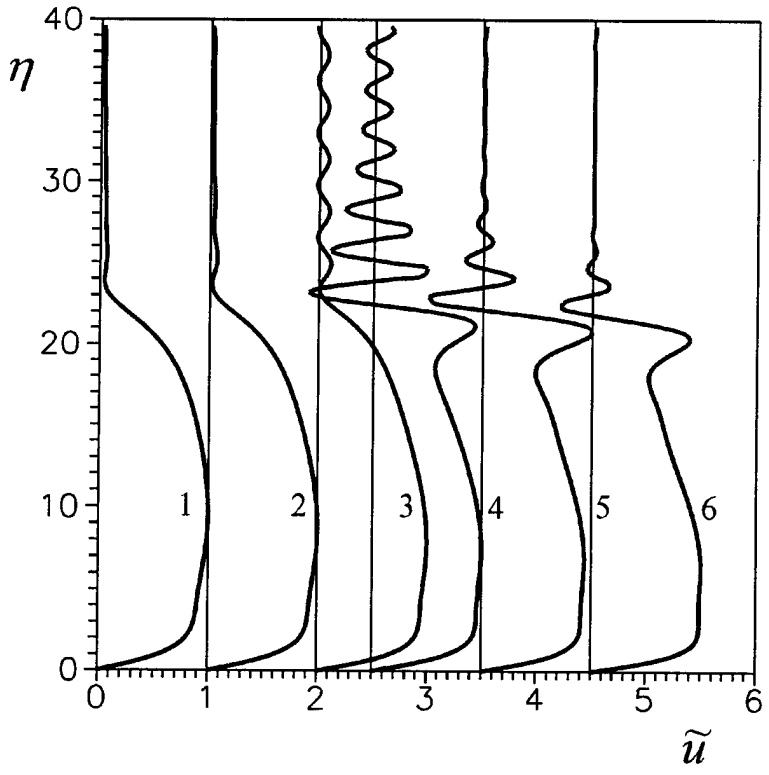

Fig. 17 First mode eigenfunctions of the x-component velocity $\tilde{u}(\eta)$ for various Reynolds numbers; 1 - $R = 1369$; 2 - $R = 1438$; 3 - $R = 1507$; 4 - $R = 1542$; 5 - $R = 1611$; 6 - $R = 1681$.

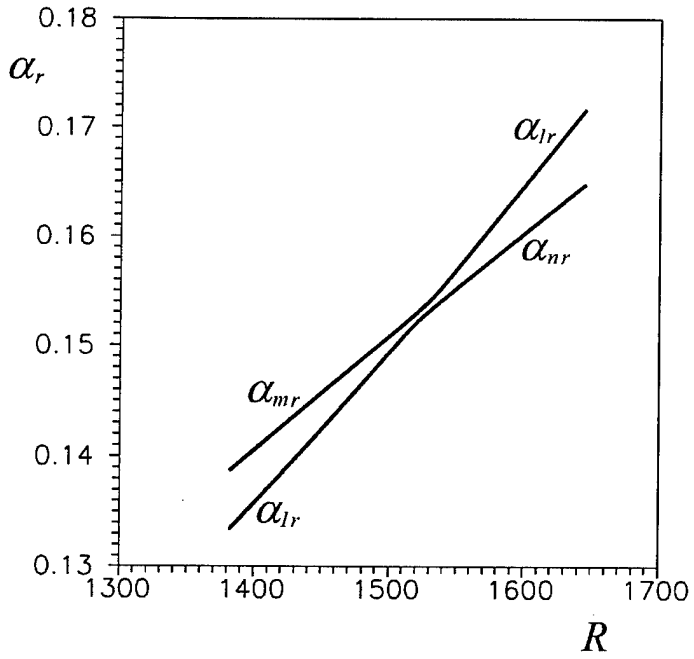

Fig. 18a Mode transformations in the synchronism region; the upper boundary $y_s^* = 4\delta^*$.

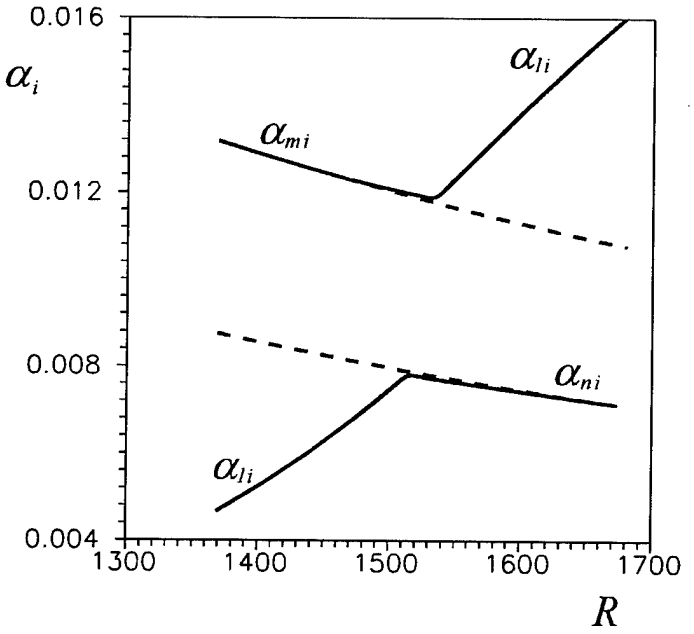

Fig. 18b Mode transformations in the synchronism region; the upper boundary $y_s^* = 4\delta^*$; dashed line - vorticity/entropy waves at $y_s \to \infty$.

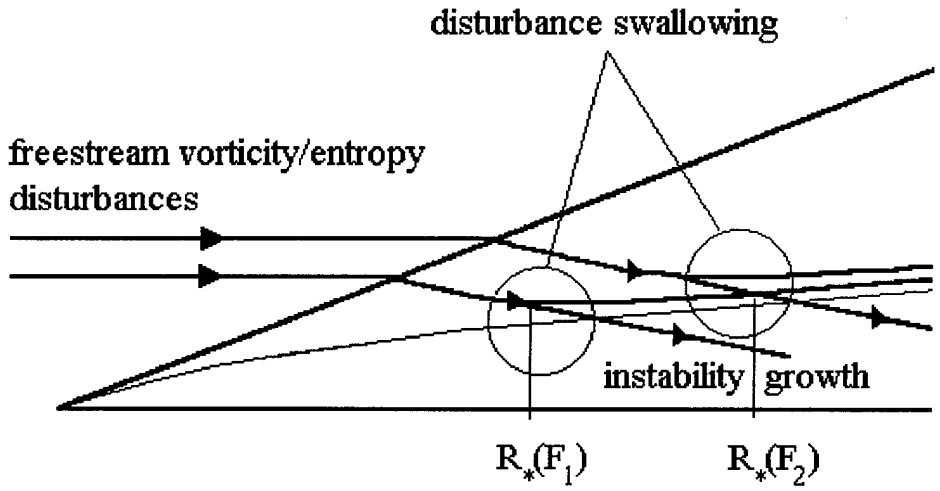

Fig. 19 Schematic picture of the freestream vorticity/entropy disturbance swallowing in synchronism regions near the points $R_*(F_1)$ and $R_*(F_2)$; frequency $F_1 > F_2$.

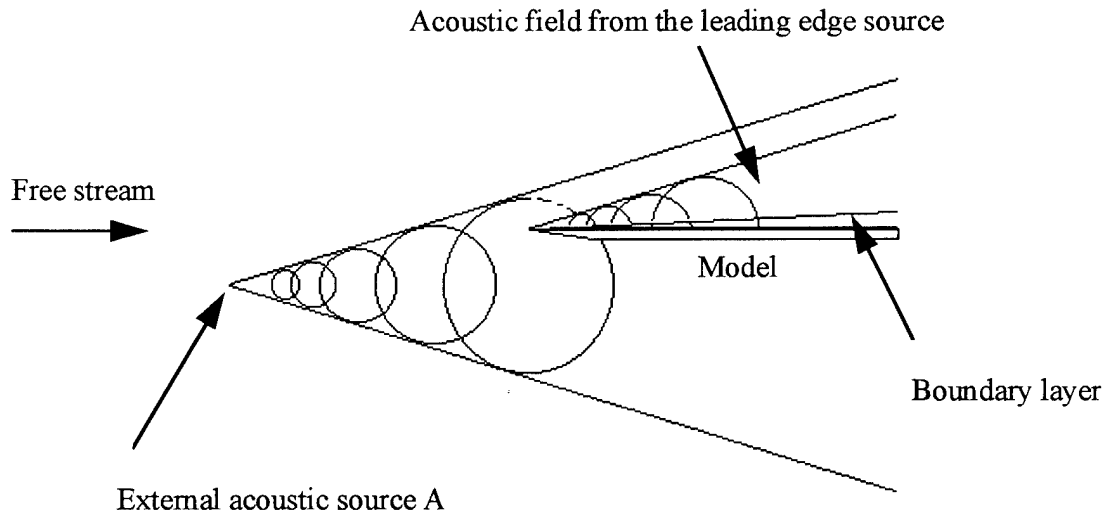

Fig. 20a Scheme of experiment with the acoustic source under control; external source (A) is below the model.

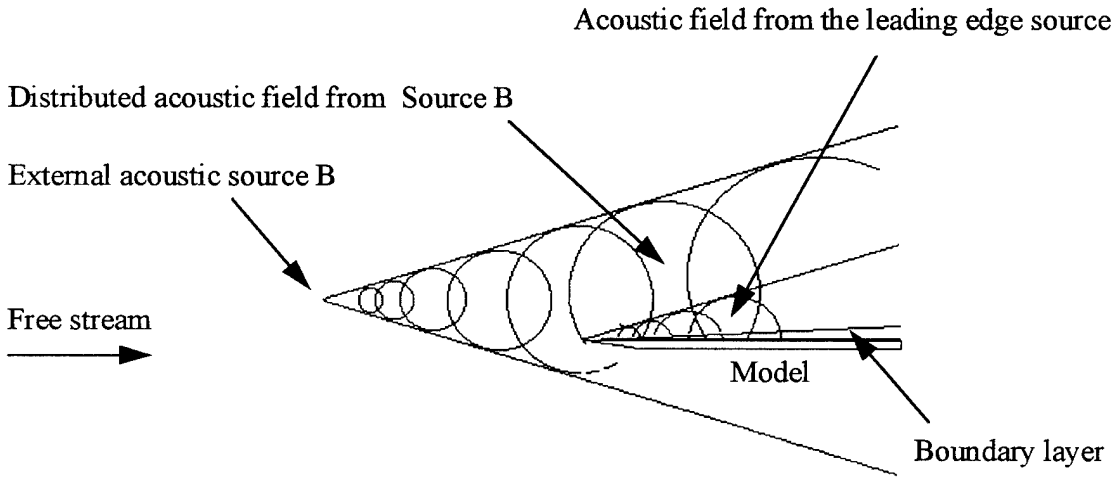

Fig. 20b Scheme of experiment with the acoustic source under control; external source (B) is above the model.